Emission of cavity coupled Rhodamine 6G dye in strong and ultra strong coupling regime

Master's thesis, 21.12.2020

Author:

Ville Tiainen

Supervisor:

Jussi Toppari

UNIVERSITY OF JYVÄSKYLÄ
DEPARTMENT OF PHYSICS

Contents

Abstract **7**

Tiivistelmä **9**

1 Introduction **11**

2 Theoretical background **15**

2.1 Light as a wave 15

2.2 Light wave at the interface of different mediums 16

2.3 Confinement of light 19

2.4 Interaction between light and matter 24

3 Experimental methods **33**

3.1 Materials and methods 33

3.2 Measurements 39

4 Results **45**

4.1 Dispersion 45

4.2 Film absorption 49

4.3 Cavity emission 50

4.4 Film emission 54

5 Conclusions **57**

A Dry film concentration **67**

B Truncated Tavis-Cummings fits **69**

Abstract

Tiainen, Ville
Emission of cavity coupled Rhodamine 6G dye in strong and ultra strong coupling regime
Master's thesis
Department of Physics, University of Jyväskylä, 2020, 70 pages.

Strong coupling between light and matter is a physical phenomen in which a confined optical mode, and a two-state system oscillating between its ground- and excited state oscillate at a common resonance frequency exchanging energy at a rate exceeding the rate at which the energy is lost from the system. This phenomen can be used to modify the the valence electron energy states of the material taking part into the coupling, and thus modify its chemical properties. This young and still for large parts undiscovered field of study is known as polariton chemistry, and the fundamental research related to it such as this thesis produce valuable information needed for the development of its practical applications.

This study follows the emission evolution of a strongly coupled system, when the coupling strength is increased from the strong coupling regime into the ultrastrong coupling regime. The coupled system consists of an ensemble of R6G-dye molecules coupled to an optical resonance mode of Fabry–Pérot cavity. The Rabi-split energies, propotional to coupling strength, determined from the samples fabricated for this thesis were 0,2518 eV, 0,4836 eV and 0,6408 eV. The emission is observed to follow the shape of the absorption of the coupled system. The measured emissions are observed to decrease in intensity as the coupling strength and molecular consentrations are increased.

Keywords: Master's thesis, Strong coupling, Ultrastrong coupling, Emission, Rabi-split

Tiivistelmä

Tiainen, Ville
Kaviteettikytketyn Rhodamine 6G väriainemolekyylin emissiotutkimus vahvan kytkennän, ja ultravahvan kytkennän alueilla.
LuK-tutkielma
Fysiikan laitos, Jyväskylän yliopisto, 2020, 70 sivua

Valon ja materian välisellä vahvalla kytkennällä tarkoitetaan tilaa, jossa yhteisellä resonanssitaajuudella värähtelevä optinen värähtelymoodi, sekä perustilan ja viritystilan välillä värähtelevä kaksitasosysteemi kykenevät vaihtamaan energiaa nopeammin, kuin systeemistä häviää energiaa. Ilmiön avulla on mahdollista muokata kytkentään osallistuvan kaksitasosysteemin valenssielektronien energiatiloja, ja sitä kautta materiaalin kemiallisia ominaisuuksia. Tämä uusi ja suurilta osin vielä tutkimaton tieteenala tunnetaan nimellä polaritonkemia, ja siihen liittyvä perustutkimus jota tämäkin tutkimus edustaa luo tärkeää ilmiön mahdollisissa käytännön sovellutuksissa tarvittavaa tietoa.

Tässä tutkielmassa seurataan vahvasti kytketyn systeemin emission kehitystä kytkentävahvuutta kasvatettaessa vahvan kytkennän alueelta ultra vahvan kytkennän alueelle. Vahva kytkentä aikaansaatiin R6G väriainemolekyylin, sekä optisen Fabry–Pérot kaviteetin avulla aikaansadun optisen resonanssimoodin välille. Tutkielmaa varten valmistetuista näytteistä määritetyt kytkentävahvuuteen suoraan verrannolliset Rabi-jakautumisenergiat ovat 2518 eV, 0,4836 eV ja 0,6408 eV. Näytteistä mitattu emissio vaikuttaa mukailevan vahvasti kytketyn systeemin absorptiota. Mittauksista havaitaan myös, että näytteestä mitattu emissio laskee systemaattisesti kytkentävahvuutta, sekä näytteen molekyylikonsentraatiota kasvatettaessa.

Avainsanat: Maisterin työ, Vahva kytkentä, Ultravahva kytkentä, Emissio, Rabi jakautuminen

1 Introduction

For centuries light and matter were considered as separate entities. Through history of mankind different civilizations and cultures have defined the building blocks of nature through their macroscopic properties and appereances. Advancements in modern science has allowed us to probe deeper from the surface into the molecular and even atomistic level. At this size scale many of the theorems of classical physics fail and a new formulation is required to explain the rich, but from the macroscopic point of view unintuitive, plethora of physical phenomenom presenting itself there. Enter quantum mechanics.

Since the dawn of quantum theory in the beginning of 20th century the distinction between light and matter has begun to blur. Quantum theory allowed the description of the interaction between a quanta of light - a photon and matter. Initially this interaction was used to explain molecular and atomic excitations where light and matter interact and weakly couple with each other, but can still be considered as separate entities. Later with the increased understanding of quantum phenomena theories evolved to include stronger light-matter coupling.

Light-matter coupling can be categorized by its coupling strength. Typically four different regimes are considered: weak coupling, strong coupling, ultrastrong coupling and deep strong coupling. The strength of the coupling can viewed as a measure of the quantum nature of the interaction where stronger coupling corresponds to increased quantum nature.

In the weak coupling regime the light-matter interaction is slower than the dissisipative processes. Therefore coherent energy transfer between light and matter is not possible and the effect of coupling is merely affecting the radiative decay rate of material. An example of such interaction is the Purcell effect [1] where the system's spontaneous emission rates can be enhanched by a resonant electromagnetic field.

Conversely in the strong coupling regime the light-matter interaction is fast enough to compete with the dissisipative processes and coherent energy transfer between the matter and light becomes possible. When light and matter strongly couple to each other they can no longer be distinquished as separate entities. New hybrid ligh-matter quasiparticles known as polaritons are formed in which light and matter both contribute to form completely new polariton states. The effect of the formation of these polariton

states is that they will change the potential energy surface of the participating material. The shape of the potential surface is an important parameter in defining the chemical reactivity of said matter, and therefore strong coupling can be used to alter the chemical properties of matter. For example it has been shown that the reaction rates of photoactive molecules can be influenced by strongly coupling the molecules [2], as well as the energy transfer rates between donor and acceptor molecules [3], [4]. It is also worth mentioning that strong coupling is not restricted to electronic excitations. Since the first experimental realization of *vibrational strong coupling* in 2015 [5] the coupling between an optical mode and vibrational excitations has evolved into a field of study of its own.

In the ultra strong coupling regime the coupling strength is strong enough to compete with the resonance and driving frequency of the system. In this regime one can observe purely quantum mechanical phenomena such as photon blockade [6], superradiant phase transitions [7] or non-classical state generation [8]. Currently this regime is a matter of great interest for scientific community. The first experimental realizations of ultra strong coupling were implemented during the last decade and many potential applications of it are being discussed and developed [9].

In the deep strong coupling regime the strength of coupling exceeds the resonance and driving frequency of the system. The phenomena taking place in this region are yet to be discovered for the most part, since experimentally this region was just reached withing the last couple of years. The current record value for the ratio of coupling strength to system resonance frequency is 1.43 [10]. The record value was achieved in between Teraherz frequency photons and inorganic metamaterial. While just reaching the deep strong coupling region has merits on its own, this kind of system is restricted in many ways. To study the effect of deep strong coupling on fluorescence for example, one would need a way to realize this kind of coupling strengths in a system containing fluorescent matter.

The first theoretical description of strong light-matter coupling was published in 1963 by Edwin Jaynes and Fred Cummings. The resulting model is fittingly called Jaynes-Cummings model [11]. The first experimental evidence of strong light-matter coupling was reported in 1975 by Yakovlev *et al.* [12] A defining moment in the light-matter coupling research occured in 1997 when a theoretical description of strong coupling between organic excitons and photons was formulated by Agranovich *et al.* [13] Agranovich's theory was put to test and verified experimentally only about a year later in 1998 when Lidzey *et al.* published their pioneering paper where they realized strong coupling with organic crystals embedded inside a microcavity.

The significance of Lidzey's achievement was not only to experimentally realize strong coupling, but to do so in room temperature enviroment with a simple cavity structure. This was made possible by the use of organic molecules which strong transition dipole moments and binding energies make them well suited candidates for strong coupling experiments. Compared to earlier experiments using complicated structures in low temperatures Lidzey's simple approach allowed an easy way to get into the strong coupling research, and sparked an evergrowing interest towards the field. Following these landmarks set by Agranovich and Lidzey *et al.* a Nobel prize in physics was awarded to Serge Haroche and David J. Wineland in 2012 for their work in light-matter coupling.

The timeline of light-matter coupling can be viewed from the perspective of number of publications. In the time of writing this text a search from the database of ScienceDirect [14] - a well known database for scientific publications yields 745733 hits with a keyword *Strong coupling*. Plotting the number of publications per year containing a keyword *Strong coupling* shows a steadily growing interest towards the phenomen. The resulting graph is shown in figure 1. The number of publications sees a noticeable rise starting from 2000 following Lidzey's 1998 paper. Another productivity boost is seen starting from 2012 when Serge Haroche and David J. Wineland were awarded their Nobel prize award.

In this thesis light-matter coupling will be studied ranging from strong coupling to ultra strong coupling regime. The coupling will be realized between optical cavity mode mode and Rhodamine 6G (R6G) organic dye molecules. The coupling strength is tuned by varying the molecular concentration of R6G while keeping the cavity parameters from sample to sample as close to each other as possible, withing the fabricational limits. In addition to dispersion measurements fluorescence of each sample is measured to study the effect of varying coupling strength on molecular fluorescence.

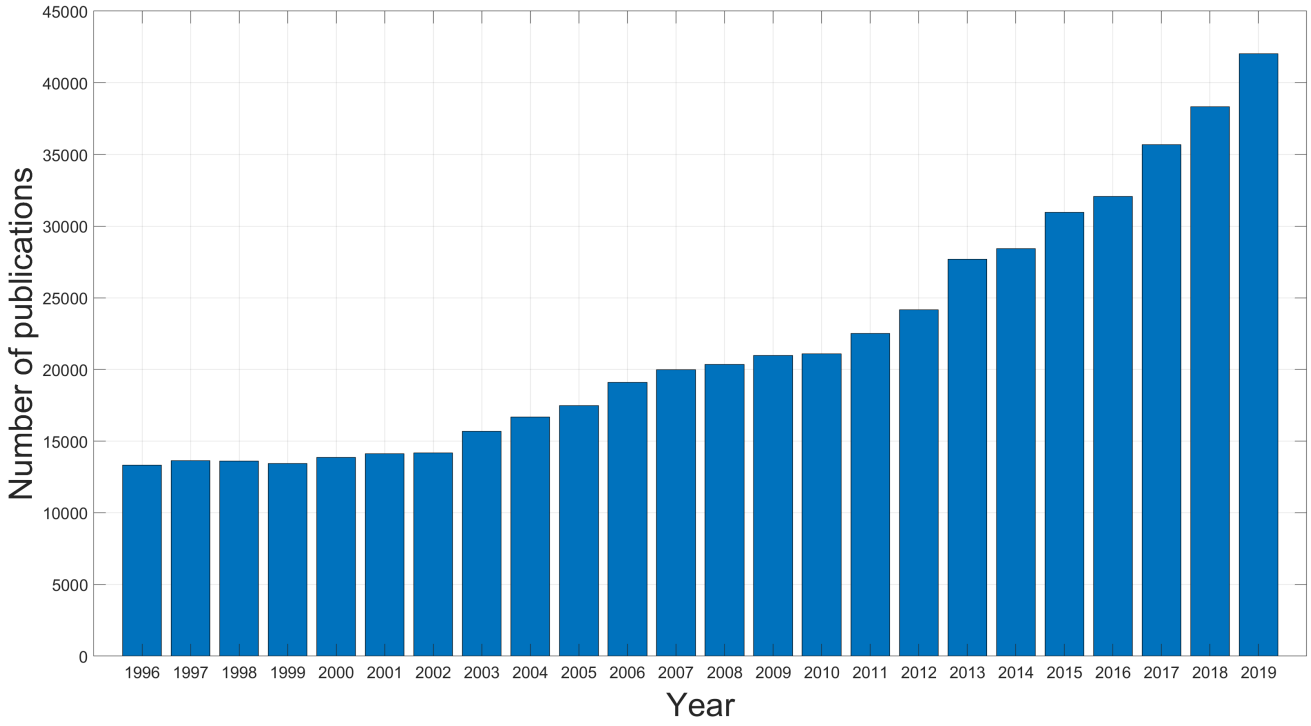

Figure 1. Number of publications by year containing a keyword *Strong coupling*

2 Theoretical background

In this chapter reader is introduced to the necessary theoretical backround to understand light-matter coupling. The chapter is divided into four parts. First a brief recap of the basic properties of light in the framework of classical electrodynamics is presented to act as foundation for the following parts. The introductory part is followed by a section explaining the behaviour of light at the interface of different mediums. After that comes a section dedicated to explaining how light can be confined into a sub-wavelength dimensions, essential necessity for the strong coupling applications. Finally the chapter ends to a section explaining the interaction between light and matter, eventually leading to a quantum mechanical model for strong coupling.

2.1 Light as a wave

Light is a form of electromagnetic (EM) radiation. This radiation can be viewed as a wave or as a collection of particles - *photons*. This dual entity of light is a concept coming from quantum mechanics known as *wave particle duality*. Which type of view we choose depends on application. When we are dealing with macroscopic properties of light, i.e., how a beam of light propagates trough different mediums it is convinient to choose the wave representation. On the otherhand when we are studying the interactions between light and microscopic entities such as molecules it is necessary to use the photon representation introduced later in this text.

In general when dealing with EM-waves one has to consider both electric- and magnetic fields. however in this study we are considering non-magnetic materials, and therefore it is sufficient to only consider the electric part of an EM-wave. Mathematical representation of the electric field part of an EM-wave is governed by a wave equation also known as the Helmholz equation [15, p. 366].

$$\nabla^2\mathbf{E}(\mathbf{r},t) + \mathbf{k}^2 n^2(\mathbf{r})\mathbf{E}(\mathbf{r}) = 0, \tag{1}$$

where $\mathbf{E}$ is the electric field, n is the refractive index of the medium, $\mathbf{r}$ is the position vector, t is the time variable, ω is the angular velocity of light, c is the speed of light and $\mathbf{k} \equiv \frac{\omega}{c}$ is the wave vector, which magnitude equals the phase velocity of the wave and

direction is telling the propagation direction of the wave. Equation 1 has an infinite set of linearly independent plane wave solutions of the form:

$$\mathbf{E} = {E_k}^0 e^{i(\mathbf{k}\cdot\mathbf{r}-\omega t)}\hat{\mathbf{e}}. \tag{2}$$

The general solution to equation 1 is then an superposition of plane waves of equation 2 with different $\mathbf{k}$ and $\hat{\mathbf{e}}$.

Whereas solutions with different $\mathbf{k}$ describe EM-waves with different propagation direction, solutions with different $\hat{\mathbf{e}}$ describe waves where the direction of electric field is different. In general $\hat{\mathbf{e}}$ must be orthogonal to $\mathbf{k}$ and we say that light is a transverse wave with transverse-electric (TE) and transverse-magnetic (TM) components. For every $\mathbf{k}$ there must be two linearly independent solutions with different $\hat{\mathbf{e}}$. The direction of $\hat{\mathbf{e}}$ defines the polarization of light. A frequently used coordinate system for polarization of light relates to the plane of incidence, which is the plane defined by the direction of the incoming propagation direction and the vector perpendicular to the plane of an interface, i.e., the plane in which the ray of light travels before and after reflection. The component parallel to the plane of incidence is called P-polarized light and the component perpendicular to this plane is called S-polarized light. In this study S-polarized light was used.

2.2 Light wave at the interface of different mediums

Imagine an TE-polarized light wave propagating in a uniform homogenous medium with refractive index n_0. What happens if the wave suddenly encounters an interface where on the other side of that interface the refractive index is different $n(\mathbf{r})$? From Maxwell's equations [15, p.356] for EM-waves we get a boundary condition: the transverse component of the electric field and its first derivative must be continuous at the interface [15, p. 392]. Adopting a cartesian coordinate system geometry where the TE-polarized light wave propagates in the z-direction the solutions for equation 1 attain the form

$$\mathbf{E} = E(z)e^{i(\mathbf{k}_\parallel\cdot\mathbf{r}_\parallel-\omega t)}\hat{\mathbf{e}}., \tag{3}$$

where the electric field $E(z)$ satifies

$$-\frac{\mathrm{d}^2E(z)}{\mathrm{d}z^2} + \left[\frac{\omega^2}{c^2}(n_0^2 - n(z)^2) - \left(\frac{\omega^2 n_0^2}{c^2} - |\mathbf{k}_\parallel|^2\right)\right] E(z) = 0. \tag{4}$$

Introducing the vacuum wavenumber $k_0 = \omega/c$ we can rewrite equation 4 as:

$$\frac{\mathrm{d}^2 E(z)}{\mathrm{d}z^2} = -(n(z)^2 k_0^2 - |\mathbf{k}_\parallel|^2)E(z) = k_0^2 n(z)^2 cos^2(\theta_n)E(z) = k_{z,n}^2 E(z), \tag{5}$$

where $k_{z,n}$ is the z-component of the wavevector of the transmitted wave inside the layer with recractive index $n(z)$, and θ_n is the angle between $\mathbf{k}$ and the normal of the interface.

Transfer-matrix method

Next we develop the formalism to model the propagation of a light wave in layered mediums. The method we adopt to do this is one frequently used in optics called the transfer-matrix method (TMM) [16]. The idea behind TMM is to take advantage of the boundary conditions for EM-field at the interface between two different mediums with different refractive indices. This means that if the E-field is known in the beginning of one layer the field at the end of this layer can be calculated with a matrix operation. Similarily the E-field through the next layer can be calculated with a different matrix. This method can be generalized to any number of layers and the resulting transfer matrix which propagates the EM-wave trough all the layers is then a product of the invidual matrices.

In the following we assume a normal incident EM-wave propagating trough a nonabsortive layered structure along z-axis. In each invidual layer the E-field is the superpostiton of forward- and backward propagating plane waves corresponding to transmitted and reflected waves:

$$E(z) = A_+ e^{ik_{z,n}z} + A_- e^{-ik_{z,n}z}, \tag{6}$$

where A_+ and A_- are the amplitudes of the electric field forward- and backward propagating waves. The transfer matrix $\mathbf{T}_n$ which relates $E(z)$ in the beginning and end of this layer must then perform the transform:

$$\mathbf{T}_n \begin{pmatrix} A_+ + A_- \\ (k_{z,n}/k_0)(A_+ + A_-) \end{pmatrix} = \begin{pmatrix} A_+ e^{ik_n a} + A_- e^{-ik_n a} \\ (k_{z,n}/k_0)(A_+ e^{ik_n a} - A_- e^{-ik_n a}) \end{pmatrix}, \tag{7}$$

Where a is the thickness of the layer. Matrix $\mathbf{T}$ which satisfies equation 7 is

$$\mathbf{T}_n = \begin{pmatrix} \cos(k_{z,n}a) & i\sin(k_{z,n}a)/(k_{z,n}/k_0) \\ i(k_{z,n}/k_0)\sin(k_{z,n}a) & \cos(k_{z,n}a) \end{pmatrix} \tag{8}$$

The system transfer matrix $\mathbf{T}_s$ which performs the transfer trough all the N layers in the

system is then a matrix product of the transfer matrices $\mathbf{T}_n$ for each invidual layers:

$$\mathbf{T}_s = \mathbf{T}_1 \cdot \mathbf{T}_2 \cdot \mathbf{T}_3 \cdot \ldots \mathbf{T}_N. \tag{9}$$

Transmission, reflection and absorption

When a propagating EM-wave encounters an object, a layer of dielectric for example, there is three possible interactions between the wave and the object. The wave can transmit trough the object, it can reflect away from the object or it can be absorbed by the object. Mathematically this can be expressed as:

$$T + R + A = 1, \tag{10}$$

where T is the intensity of the wave that is transmitted and R and A are correspondingly the intensities that are reflected and absorbed. Experimentally it is very difficult to measure the portion that is absorbed so the usual practice is to measure the transmitted and reflected portions of the incident wave and use equation 10 to calculate A.

To design optical systems one needs to also be able to calculate T and R. This can be done using the Fresnel coefficients derived by Augustin Fresnel in 1866-1870. Fresnel who lived in a time before Maxwell's equations had a vastly different idea of EM-wave of that what we have today. He thought light as a transverse *mechanical* wave. Instead of boundary conditions imposed by Maxwell's equations he used the idea that as a transverse mechanical wave is propagating trough an interface the materials on both sides of the interface should not slip past or detach from each other. With this mechanical approach he was able to explain the polarization effects along with the variations in reflectance and transmittance as the function of incident angle with such precision that the same formulation is still being used today.

Fresnel compared the ratios of reflected and transmitted wave's aplitudes to that of incident wave. These ratios are called the Fresnel's coefficients r and t [17] for reflected and transmitted waves correspondingly. In the case of s-polarized light these can be written as:

$$\begin{cases} r \equiv \frac{{E_r}^{(s)}}{{E_i}^{(s)}} = \frac{n_i\cos(\theta_i) - n_t\cos(\theta_t)}{n_i\cos(\theta_i) + n_t\cos(\theta_t)} \\ t \equiv \frac{{E_t}^{(s)}}{{E_i}^{(s)}} = \frac{2n_i\cos(\theta_i)}{n_i\cos(\theta_i) + n_t\cos(\theta_t)} \end{cases}, \tag{11}$$

where n_i and n_t are the refractive indices of the mediums in which the incident and transmitted waves travel, θ_i and θ_t are correspondingly the angle of incidence and angle of transmitted wave as measured from the propagation axis.

Since r and t give us the relative *amplitudes* of reflected and transmitted waves and we are interested in *intensities* of these waves we need to do a conversion from amplitude to intensity. Gladly this is an easy task, since intensity is propotonial to the square of amplitude, so by knowing r and t allows us to calculate R and T directly:

$$R \equiv |r|^2 \quad and \quad T \equiv |t|^2. \tag{12}$$

2.3 Confinement of light

There are several ways how light can be confined into dimensions smaller than the light's own wavelength. The most commonly used methods for confining light in the visible range are plasmonic- and optical- cavities. For the purposes of this study optical Fabry–Pérot cavity was chosen.

Fabry–Pérot cavity

Fabry–Pérot cavity is the most basic optical resonator which can be used to confine light. It consist of two parallel plane mirrors separated by a layer of dielectric material. A schematic figure of such a device is shown in figure 2a.

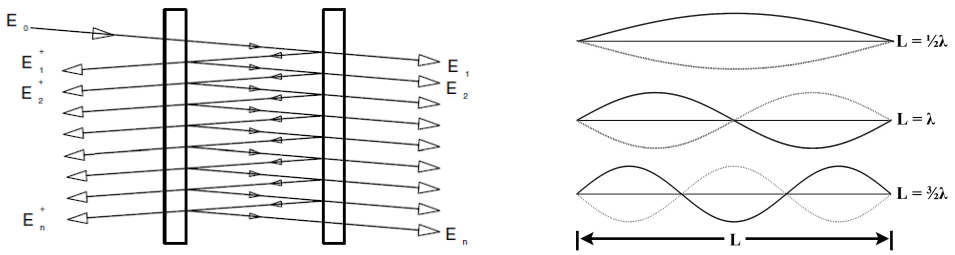

(a) Fabry–Pérot cavity [18]. **(b)** Cavity modes.

Figure 2

When a ray of light is projected towards the cavity and faces the first mirror it is subjected to a probability test. Part of the light is reflected back from the first mirror, and part is transmitted trough the first mirror into the dielectric inside the cavity. Inside the cavity the light ray continues on its path until it faces the second mirror. There it can again either reflect back inside the cavity, or transmit trough the second mirror and escape from the cavity. The part of light which was reflected back into the dielectric travels back to the first mirror. There it can again either reflect or transmit trough the first mirror and escape the cavity. The part which was reflected back into the cavity starts the cycle again.

When there are many light waves bouncing back and forth inside the cavity they will interfere with each other. This interference will be either destructive or constructive. The effect of this interference is that the constructively interfering light wavelengths will get amplified and destructively interfering wavelengths will dissappear from the cavity. The constructively interfering wavelengths will create standing electro-magnetic (EM) waves with resonant modes inside the cavity. The resonance condition occurs when the length of the cavity L_{cav} [1] i.e the distance between the two mirrors is an integer number of intracavity half wavelengths:

$$L_{cav} = \frac{m\lambda}{2n} \qquad m \in \mathbb{N}, \tag{13}$$

where λ is the wavelength of light and n is the refractive index for the dielectric inside the cavity. For a given cavity length L_{cav} many resonant modes can form inside the cavity. These modes are spaced $\frac{\lambda}{2}$ apart. The first 3 modes for intracavity EM-fields are depicted in figure 2b.

From spectroscopic point of view the formation of these cavity modes means, that at certain resonance wavelenths the incident light will be absorbed by the cavity. [2] With the combination of TMM and Fresnel coefficient's we can calculate the optimal cavity parameters (layer thicknesses and materials) to have higly absorptive cavities at the chosen wavelength. As an example figure 3 represents the calculated absorpion spectrum of a silver mirror cavity with polyvinyl alcohol (PVA) used as a spacer layer between the mirrors.

[1] The expression for L_{cav} is valid only in ideal situation, where the cavity mirrors are considered to be perfect mirrors reflecting all of the incident light. In reality some of the light will penetrate the mirrors, effectively broadening the resonance bandwidth and shifting the resonance peak.

[2] Here one has to be careful on how to interpret the word *absorbed*. Normally when absorption is considered in the context of photons it is assumed that the photon's energy is absorbed and used in some process. Viewing the cavity from outside as an isolated system it certainly looks like if the photons are being absorbed but in reality the photons are merely stored inside the cavity retaining their energy.

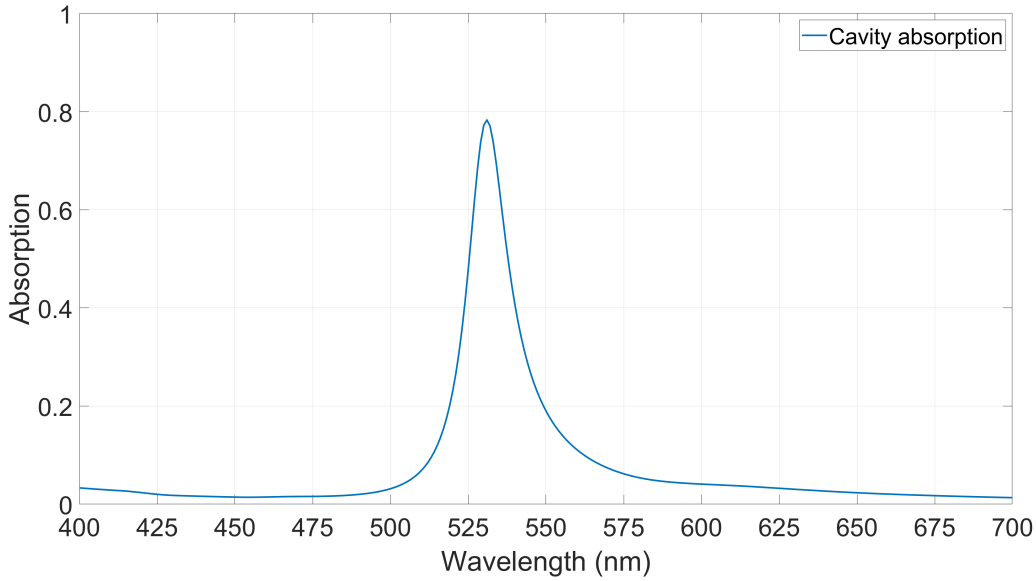

Figure 3. Absorption of a silver mirror cavity calculated using TMM for s-polarized light. Thickness of the mirror facing the incident light is 30 nm, 130 nm for the PVA layer and 200 nm for the second silver layer. After 200 nm silver layer there is a semi-infinite piece of BK7 glass. The medium surrounding the cavity is air.

Quality factor and mode volume

The two important parameters used to quantify the confinement of light in any resonant structure are quality factor (Q) and mode volume (V_m). Q is a measure of how long the light stays trapped inside the confining stucture - in other words it measures *temporal* confinement. There are two commonly used ways to define Q for a resonant structure [19]. First definition uses the ratio of energy stored E_{stored} in the resonator to energy lost from the resonator per oscillation cycle $E_{dissipated}$:

$$Q = 2\pi \frac{E_{stored}}{E_{dissipated}}, \tag{14}$$

where the factor of 2π comes from the fact that we are considering the amount of energy stored in the structure during one full oscillation cycle. Another definition for Q uses the ratio of resonance frequency f_r to full width half maximum (FWHM) of the resonance bandwidth σ_f:

$$Q = \frac{f_r}{\sigma_f}. \tag{15}$$

While the definition for Q given in eq. 14 is very robust it is a bit cumbersome to use for experimentalist, since measuring stored and dissipated energies directly inside the cavity is a formidable task. Q given by the alternative definition in eq. 15 however is by contrast

easily determided by a simple spectroscopic measurement, and hence better suited for experimentalists. Whereas the practical use of eq. 14 is somewhat limited, it does give a good intuition for the meaning of Q. If we imagine a perfect cavity which doesn't leak any light and is able to store it infidently Q would be infinite. This is exactly what equation 14 tells us: for infinite Q the term $E_{dissipated}$ has to approach zero. In other words all of the incident light is stored inside the resonant structure, while nothing is dissipated. In spectroscopic terms of eq. 15 a similar ideal case would mean that the bandwidth of the resonance mode would similarly approach zero.

Whereas Q is a measure of *temporal* confinement of light V_m is a measure of *spatial* confinement of light. The term mode volume was first introduced by Edwin M. Purcell in his 1946 paper in the context of spontaneous emission [20]. In Purcell's words: *"V is the volume of the resonator. ... If a is a dimension characteristic of the circuit so that* $V \sim a^3$ *"*. The vague definition of mode volume proposed by Purcell has later been replaced by more rigorous definitions using volume integral of the electric field intensity in and around the confining structure, normalized to the maximum field intensity. Although the definition and expression of mode volume has improved over the years still no universal expression for it exist [21]. In the context of this thesis, the absolute value of mode volume of the cavity is not considered. Although mode volume V_m plays an important role in strong coupling (see eq. 29) we are assuming that all of the cavity parameters, including V_m are identical in all of the samples studied in this thesis work. Because of this assumption the measurement data from the samples used for this study are comparable even if the absolute value of V_m remains unknown.

Cavity dispersion

The system transfer matrix in equation 7 depends on the k-vector of the incident wave. As $k_{z,n} = k_0 n(z)\cos(\theta_n)$ in turn depends on the incident angle θ_n it is clear that the transmission and reflection and hence absorption of the cavity has angular dispersion.

Most of this effect is due to the changes in the wave's phase factor inside the cavity. As the incident angle is increased the stop band of the cavity moves up to higher energies causing the cavity resonance to move over into higher energy. The energy of an optical cavity is given approximately by [22, p. 941 eq. 12]

$$E_c(k_\parallel) = \frac{\hbar c}{n_c}\sqrt{\left(\frac{m\pi}{L_{cav}}\right)^2 + \left(\frac{2\pi}{\lambda}\sin(\theta_n)\right)^2}, \tag{16}$$

where n_c is the refractive index in the medium surrounding the cavity.

The effect of increasing cavity energy with increasing incident angle is demonstrated in figure 4 where TMM is used to simulate the cavity with the same parameters as in figure 3 with varying incident angles.

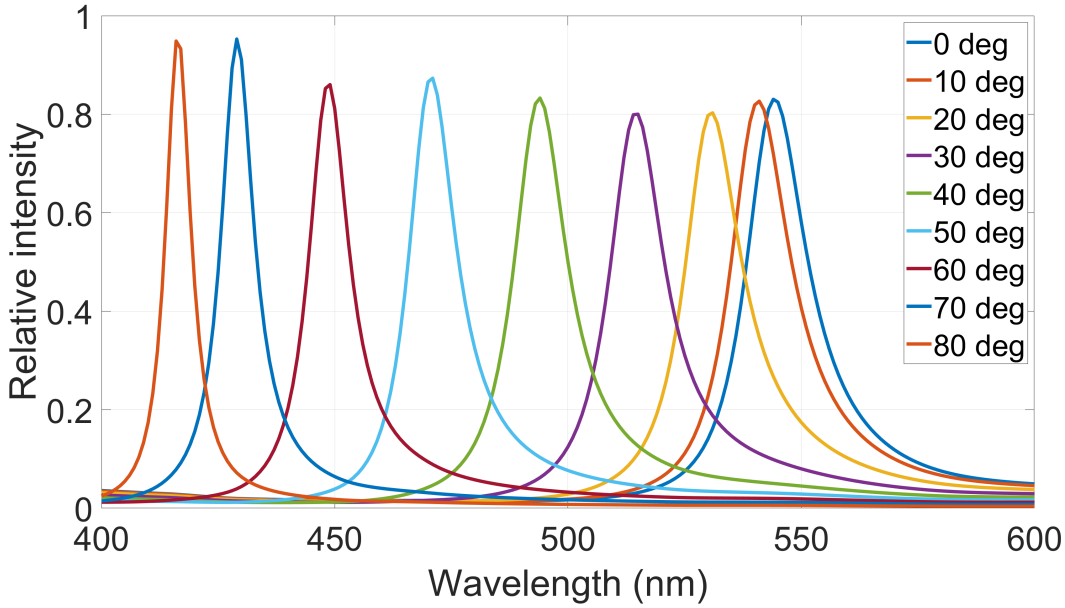

Figure 4. Absorption of a cavity as presented in figure 3 simulated using varying incident angles.

Another perhaps more informative way of visualizing the cavity dispersion is the dispersion curve. Such a curve is presented in figure 5 where the resonant wavelengths are plotted against the incident angle [3].

[3]There are multiple ways in which dispersion curves are presented. The most commonly used one maps the resonant energies against inplane k-vector. In this presentation the y-axis values are flipped, and the resulting graph is a mirror image of what is seen in figure 5. A different presentation was chosen here to be consistent with rest of the text.

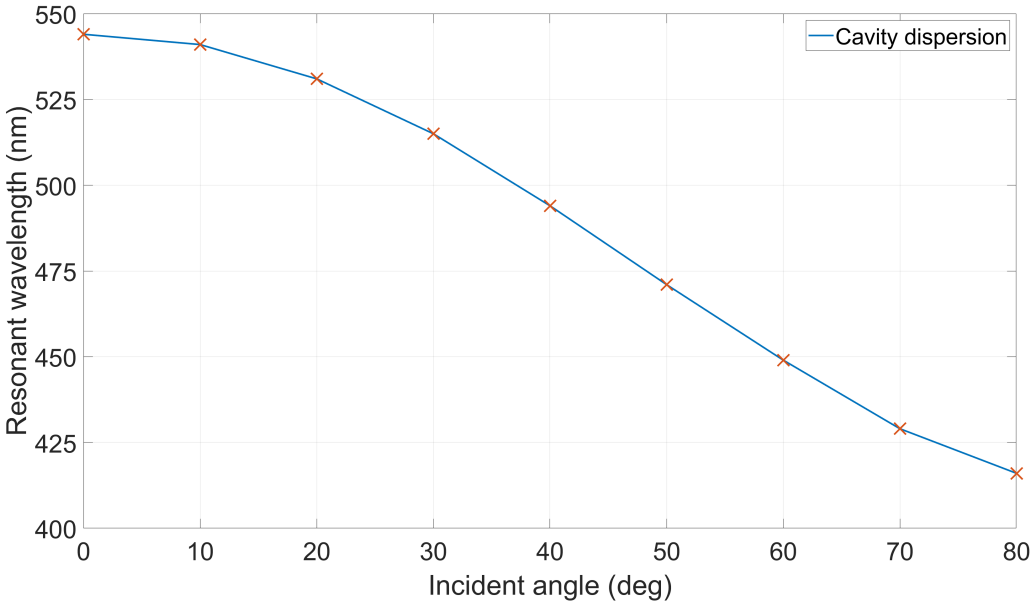

Figure 5. Dispersion curve exctracted from the peak values of figure 4

The great benefit of using dispersive cavities in strong coupling applications is that they are *tunable*. With TMM it is very straightforward to design a cavity with absorption maximum wherever we need it. Realizing this design experimentally however requires a fabrication process where the cavity layer thicknesses are needed to be controllable up to a nanometer accuracy. Cavity dispersion is a remedy here since it allows us to have the thicknesses few nanometers off and still have the absorption maximum where we need it just by tuning the incident angle.

2.4 Interaction between light and matter

So far we have covered the basic properties of light, and how it can be confined into subwavelength scale. Next step in the journey to understand strong coupling phenomen is to have an idea how light and matter can interact. The strategy that we adopt to do this consists of three steps. First we see how quantized EM-field can be treated as a collection of harmonic oscillators. In the second step we convince ourselves that in a similar fashion an ensemble of atomic two state systems interacting with uniform EM-field can be considered as a collection harmonic oscillators. Finally we introduce the quantum description of strong coupling treating light and matter as coupled harmonic oscillators.

Quantization of EM-field

To treat the EM-field as a collection of particles instead of continuous vector field is equivalent to saying that the EM-field is quantized. These discrete particles each carrying a quanta of EM-radiation, which together constitute the EM-wave, are photons. The energy of a single photon can be calculated with the famous Planck-Einstein relation:

$$\epsilon_p = \frac{hc}{\lambda}, \tag{17}$$

where λ refers to the wavelength of an EM-wave as presented in the wave representation.

The leap from continuous fields to discrete particles might seem counterintuitive at first, but already in equation 2 we saw how electric field can be separated into a collection of plane waves each having a different k-vector, where plane waves with different k-vector represent the normal modes of the EM-field with different oscillation frequencies and corresponding energies. This separation was done completely withing the framework of classical electrodynamics resulting from the requirement to satisfy Maxwell's equations. Following this path further it can be shown that the Hamiltonian of the system is of the form of Hamiltonian of a mechanical harmonic oscillator with E-field being analogous to the position- and B-field analogous to the momentum of the mechanical oscillator. Using this classical analogy as a guideline it is possible to deduce the appropriate quantum mechanical operators to treat the EM-field as a collection of J modes of quantum harmonic oscillators with Hamiltonian of a j:th mode having form:

$$H_j = \hbar\omega_j(a_j^\dagger a_j + \frac{1}{2}) = \hbar\omega_j(\hat{n} + \frac{1}{2}), \tag{18}$$

where $a_j^\dagger$ and a_j are the creation and annihilation operators of the j:th photon correspondingly and $\hat{n}$ is the number operator specifying the number of photons in this state. In the case of an optical cavity like the Fabry–Pérot cavity discussed earlier in this text the strength of the electric field associated with a single photon of the j:th mode is given by [23]:

$$E_{ph} = \sqrt{\frac{\hbar\omega_j}{2\epsilon_0 V_m}}, \tag{19}$$

where ϵ_0 is the vacuum permittivity.

A noteworthy difference in the Hamiltonian shown in eq. 18 as compared to the Hamiltonian of classical harmonic oscillator is the ground state energy. In classical case it is possible for the oscillator to be at rest, i.e., to have zero kinetic- and potential energy simultaneously. On the contrary in eq. 18 the ground state energy is atleast $\hbar\omega_0/2$ even

in the presense of no photons at all. This zero point energy is a consequence of Heisenberg uncertainty principle which forbids the simultaneous vanishing of kinetic- and potential energy. In this ground state there also excists a corresponding ground state E-field, called the vacuum field. Again in the case of an optical cavity vacuum field is [22, eq. 4]:

$$E_{vac} = \sqrt{\frac{\hbar\omega_c}{2\epsilon_0 V_m}}, \tag{20}$$

where ω_c is the charecteristic cavity resonant frequency. When interacting with atomic systems, this vacuum field and atomic system may couple causing a pure quantum phenomen known as vacuum Rabi oscillation, as well as act as an reservoir for the decay of atomic system [24].

Two level atomic system interacting with uniform EM-field

It is easy to imagine how charged particles or ionic compounds having a net electrical charge can interact with electric field via Coulumb interaction. However as in general stable molecules are charge neutral it might be suprising that Coulombic interactions are still responsible for the light-matter interactions even if the net charge of molecule is zero. When charge neutral molecule encounters an electric field the electrons bound into the nuclei rearrange themselves to counter this external field. As a result even though the molecule remains uncharged the molecule develops an electric dipole with effective locally distributed net charge. Trough this dipole the molecule is able to interact with the electric field, and possibly exchange energy with it via photon absorption or emission if accessible transition matching the energy of the photon is available. The likelyhood of energy exchange occuring between the electric field and the molecule is determined by the expectation value of transition dipole moment operator $\hat{d}$:

$$d_{i\to f} = \langle \Psi_f | \, \hat{d} \, | \Psi_i \rangle \,, \tag{21}$$

where Ψ represents the molecular state, and the subscripts i and f are used to specify initial- and final states correspondingly. As $\hat{d}$ varies from molecule to another some molecules are better absorbers/emitters than others and therefore better suited for strong coupling applications requiring strong light-matter interaction. The strength of coupling between electric field and molecular dipole is given by the interaction energy V:

$$V = -\hat{d} \cdot \hat{E}, \tag{22}$$

where $\hat{E}$ is the electric field operator. Worth of note is the dot product between $\hat{d}$ and $\hat{E}$ in eq. 22 which implies that the relative orientation of the molecules and electric field affects the strength of coupling.

The rate at which the molecular transitions induced by the electric field take place can be estimated with Fermi's golden rule giving expression for the transition rate Γ:

$$\Gamma = \frac{2\pi}{\hbar}|\hat{d} \cdot \hat{E}|^2 \rho(\epsilon), \tag{23}$$

where $\rho(\epsilon)$ is the density of states (DOS) of the coupled EM-field at energy ϵ.

From eq 23 it is clear that DOS has a significant effect on Γ. In light confining structures, such as the Fabry–Pérot cavity introduced earlier, DOS is increased significantly compared to free space DOS at the energy corresponfing to the resonant frequency of the cavity. If the cavity frequency is tuned to match the molecular transition frequency a drastic change can be observed in the transition rate. A manifestation of this effect increasing the rate of spontaneous emission is known as the Purcell effect [1]. Intuitively this effect of increasing transition rate along with increasing DOS can be undestood by thinking the situation from the perspetive of a single intracavity photon. When a molecule emits a photon inside the cavity there is a good change that the photon will reflect from the cavity mirror back into the cavity as was described in section 2, effectively increasing the photon DOS inside the cavity as compared to the free space. Furthermore this gives the photon an opportunity to be reabsorbed by another molecule causing another transition, and thus increasing the transition rate. If the probability for the photon to be reabsorbed is less than the probability sum of all the competing processes by which the photon may exit the cavity then the light matter coupling is said to be weak, and besides having an effect on the molecular transition rate the coupling has no other effects on the molecule. On the contrary if the reabsorbtion probability is higher than the probability sum of all the competing dissisipative processes, then the system may enter into the strong coupling regime, where interesting new physical phenomena arising from the coupling may be observed.

Coupled harmonic oscillators - the formation of polaritons

So far we have seen how the quantized electric field can be modelled as a collection of modes, each represented by harmonic oscillator. We also saw how this field can exchange energy with a two state system at a rate determined by eq 23. If the rate is sufficiently fast to compete with the dissisipative processes such that the intracavity photon can have multiple absorption-emission cycles before exiting from the cavity the interaction can be considered as an interaction between two coupled oscillators where energy is exhanged between the cavity mode and the two state system.

To justify the coupled harmonic oscillators (CHO) model we need to make few approximations. First of all real molecules have broad absorption- and emission spectra instead of sharp well defined transitions that we assume when we consider a two state system. Despite this idealization the model is able to capture the important physics even if we only consider the maximum values of the absorption peaks when determining the transition energies. Second approximation that we make is the dipole approximation [25]. Here we consider the electric field to be uniform and homogenious in the proximity of the molecule, which allows us to consider the coupling solely trough dipole interactions between electric dipole and uniform electric field, as we did in the previous section. To justify this approximation the wavelength of the coupled electric field mode needs to be greater than the molecular size, by orders of magnitude. For visible light with wavelengths in the order of hundreds of nanometers and organic molecules with a length scale of about ten nanometers [26] this approximation is well justified. Given these approximations interaction energy of eq. 22 becomes [23]:

$$\begin{aligned} V &= -\sum_{\alpha}(\hat{E}_{\alpha} + \hat{E}_{\alpha}^{\dagger}) \cdot (\hat{d}\,|1\rangle\langle 0| + \hat{d}^{*}\,|0\rangle\langle 1|) \\ &= \sum_{\alpha}\sum_{j}\sqrt{\frac{2\pi\hbar\omega_j}{V_m}}(a_j^{\dagger}e^{-i\hat{k}_j\cdot\hat{r}} + a_j e^{i\hat{k}_j\cdot\hat{r}})(d_{\alpha}\,|1\rangle\langle 0| + d_{\alpha}^{*}\,|0\rangle\langle 1|), \end{aligned} \tag{24}$$

where sum over α accounts for the two possible polarizations and states 0 and 1 correspond to the ground- and first excited states of the molecule. Equation 24 contains four terms. The terms and their physical significance can be summarized as:

$a_j^{\dagger}\,\|0\rangle\langle 1\|$	Molecule decays from $\|1\rangle \rightarrow \|0\rangle$ and emits a photon (in the j^{th} mode)
$a_j\,\|1\rangle\langle 0\|$	Molecule is excited from $\|0\rangle \rightarrow \|1\rangle$ and absorbs a photon (in the j^{th} mode)
$a_j^{\dagger}\,\|1\rangle\langle 0\|$	Molecule is excited from $\|0\rangle \rightarrow \|1\rangle$ and emits a photon (in the j^{th} mode)
$a_j\,\|0\rangle\langle 1\|$	Molecule decays from $\|1\rangle \rightarrow \|0\rangle$ and absorbs a photon (in the j^{th} mode).

Going to the interaction frame (Dirac picture) allows us to see how the interaction energy varies over time. The standard treatment adds time depependant factor $e^{\pm i\omega_j t}$ to each mode, and a corresponding $e^{\pm i\omega_m t}$ term to the molecule transforming the four terms in the interaction energy to:

$$\begin{aligned}
a_j^\dagger \left|0\right\rangle \left\langle 1\right| \quad &\rightarrow \quad a_j^\dagger \left|0\right\rangle \left\langle 1\right| e^{i(\omega_m-\omega_j)t} \\
a_j \left|1\right\rangle \left\langle 0\right| \quad &\rightarrow \quad a_j \left|1\right\rangle \left\langle 0\right| e^{-i(\omega_m-\omega_j)t} \\
a_j^\dagger \left|1\right\rangle \left\langle 0\right| \quad &\rightarrow \quad a_j^\dagger \left|1\right\rangle \left\langle 0\right| e^{i(\omega_m+\omega_j)t} \\
a_j \left|0\right\rangle \left\langle 1\right| \quad &\rightarrow \quad a_j \left|0\right\rangle \left\langle 1\right| e^{-i(\omega_m+\omega_j)t},
\end{aligned}$$

where ω_m is the transition frequency of the molecule. From the interaction frame we can see that close to the resonance condition ($\omega_j \approx \omega_m$) only the two first terms are significant, while the last two terms oscillating at a much faster frequency quickly average to zero. This leads us to the rotating wave approximation (RWA) valid for systems close to the resonance with coupling strengths in the strong coupling regime, allowing us to neglect these fast rotating terms [27].

Within the RWA the interaction energy can be solved analytically, for the system consisting of a single two-level molecule interacting with a single mode of an EM-field. The single mode of the EM-field that we consider troughout the rest of this text is the confined cavity field mode, strength of which is given by eq. 19. This system is described by the Jaynes-Cummings hamiltonian [11]:

$$\hat{H}_{JC} = \hat{H}_{mol} + \hat{H}_{cav} + \hat{H}_{int} = \frac{1}{2}\hbar\omega_m\hat{\sigma}_z + \hbar\omega_c(\hat{a}^\dagger\hat{a} + \frac{1}{2}) + \hbar g_0(\hat{a}^\dagger\hat{\sigma} + \hat{a}\hat{\sigma}^\dagger), \qquad (25)$$

where $\hat{\sigma}_z$, $\hat{\sigma}$ and $\hat{\sigma}^\dagger$ are the Pauli matrix and raising- and lowering operators respectively and g_0 is the coupling energy measuring the strength of the light-matter coupling between single two-state system and EM-field mode. In the limit of large number of molecules and small number of photons this model can be extended to cover N molecules instead of just one by using the Tavis-Cummings Hamiltonian [22, eq. 9]:

$$\hat{H}_{TC} \cong \hbar\omega_m(-\frac{N}{2} + \hat{b}^\dagger\hat{b}) + \hbar\omega_c\hat{a}^\dagger\hat{a} + \hbar g(\hat{a}^\dagger\hat{b} + \hat{a}\hat{b}^\dagger), \qquad (26)$$

where $\hat{b}^\dagger$ and $\hat{b}$ are the bosonic creation- and annihilation operators obtained by the Holstein–Primakoff transformation [28]. The main difference between $\hat{H}_{JC}$ and $\hat{H}_{TC}$ is that while the first is considering only one coupled two-state system the latter treats the molecular excitation as delocalized excitation where the excitation energy is shared among

all of the N molecules treating the system as one giant quantum harmonic oscillator with a total of $N+1$ states (N molecular states + 1 cavity mode state). The delocalized nature of excitation also has an effect on the coupling strength. The collective coupling strength g is proportional to the square root of N:

$$g = g_0\sqrt{N}, \tag{27}$$

implying that the amount of molecules participating in coupling is having a great effect on coupling strength. As we saw from eq. 19 the electric field strength inside the cavity is proportional to $\sqrt{V_m^{-1}}$, and as g_0 is proportional to that it becomes clear that the magnitude of g is actually affected by the number of molecules inside the mode volume V_m. In other words the strength of collective coupling is determined by the molecular *concentration*. A truncated Tavis-Cummings model which is a simplification of equation 26 can be presented in matrix form as [22, eq. 15]:

$$\hat{H}_{TC} = \begin{bmatrix} \epsilon_c(\lambda) & \frac{\hbar\Omega_R}{2} \\ \frac{\hbar\Omega_R}{2} & \epsilon_m \end{bmatrix}, \tag{28}$$

where ϵ_c is the energy of the cavity mode as a function of wavelength, ϵ_m is the transition energy of the intracavity molecules and Ω_R is the Rabi-split given by:

$$\Omega_R = 2\hbar g = 2d\sqrt{N}\sqrt{\frac{\hbar\omega_c}{2\epsilon_0 V_m}} \tag{29}$$

Equation 28 can be diagonalized yielding two eigenstate energies:

$$\epsilon_\pm(\lambda) = \frac{\epsilon_c(\lambda) + \epsilon_m}{2} \pm \sqrt{(\hbar\Omega_R)^2 + (\epsilon_c(\lambda) - \epsilon_m)^2}. \tag{30}$$

These eigenenergies belong to the eigenstates of the coupled system which are linear combinations of pure light- and matter states usually called *polaritons*. The upper (+) and lower (-) polaritons are equally spaced $\pm\hbar g$ from ϵ_m. The energy difference between the polariton states is at its minimum when the system is in resonance, i.e., $\epsilon_c(\lambda)$=ϵ_m. In this state the light-matter state mixing is at its maximum and the system is acting as 50/50 hybrid of light and matter. In resonance an avoided crossing is observed between the eigenenergies. This avoided crossing is called Rabi-split, magnitude of which is given by equation 29.

Rest of the $N-1$ eigenstates of the system are called *dark-states*. They are called so because they are almost purely molecular excitation states lacking significant cavity

contribution, and as such they are far less visible compared to the polaritonic states. As these states are located between upper- and lower polariton states they provide a path for relaxation from upper- to lower polariton. The truncated Tavis-Cummings model introduced in equation 28 is simplifying equation 26 by dismissing these dark states, and is considering only the two polaritonic states.

Classification of coupling strength

Now that we have an idea of what is meant by light-matter coupling we need some way to classify the different regimes of light-matter coupling. Unfortunately no universally accepted definition excists for these regimes. There are five important parameters defining Rabi-like systems: ω_c of the confined electric field, material dependant transition frequency ω_m, coupling energy g, decay rate of the confined photons κ and decay rate of the material exciton γ. As the different arrangements of these parameters are driving the physics in different regimes it is necessary to consider each of them in the context of their corresponding regime. The classification that we follow here defines the different regimes of coupling strength as follows [29]:

- In the *weak coupling regime* $g \ll \gamma, \kappa, \omega_c, \omega_m$.
- In the *strong coupling regime* $\gamma, \kappa \ll g \ll \omega_c, \omega_m$.
- In the *ultra strong coupling regime* $\frac{g}{\omega_c} > 0.1$.

As we can see from the above definitions, in the regimes from weak- to strong coupling the decay rates are in central role. However in the ultra strong coupling regime only the ratio between the resonant field frequency and coupling energy is considered. In some literature sources it has been proposed that if the considered system has high decay rates this can lead to a situation where the system is classified to be in the ultra strong coupling regime, without having strong coupling in the first place [30]. In addition to the above mentioned regimes, there also excists regions of even higher coupling strengths, where even more new physical phenomen can be observed due to the stronger coupling between light and matter. In the context of this thesis the studied coupling strengths range from strong- to ultrastrong, so regions above ultra strong are outside the scope of this text. A reader interested in the physics of those regions is advised to see an excellent Nature review article mainly focused on ultra strong coupling, but also extending beyond that in theory and simulations [30].

3 Experimental methods

In this chapter a detailed description of experimental methods used in this thesis is given. The chapter is divided in two sections. In the first section the reader is introduced to the materials and methods used to fabricate the samples. The second section is dedicated to presenting the measurement setup used in this thesis and the performed measurements.

3.1 Materials and methods

A total of seven samples were fabricated for the purposes of this thesis. The total number of samples includes three cavity samples with a molecule doped middle layer, and one cavity sample with the middle layer made of just polymer without any active molecules. In addition to the cavity samples three simple film samples were fabricated to act as uncoupled reference systems for the cavity samples with corresponding molecule concentrations. The cavity samples are labeled from low to high R6G concentration as C1,C2 and C3. The corresponding film samples are labeled as F1,F2 and F3. Between each sample the R6G concentration is increased by a factor of three. The empty cavity reference system without R6G is referred as C4.

Materials and sample design

The most important choice of material affecting every other choice related to the experimental part of this thesis was the choice of active molecule used in the "material" part of the pursued light-matter coupling. The molecule that was chosen is named *Xanthylium, 9-[2-(ethoxycarbonyl)phenyl]-3,6-bis(ethylamino)-2,7-dimethyl-, chloride* commonly known as Rhodamine 6G (R6G). R6G is a highly fluorescent strong red coloured organic dye, commonly used for scientific purposes such as imaging applications and dye lasers. R6G has high transition dipole moment making it a good candidate for strong coupling applications. Its absorption maximum occurs at ~ 532 nm with a shoulder peak located at ~ 495nm. The fluorescence emission maximum is located at ~ 570nm giving a Stokes shift of approximately 40 nm. The locations of maxima can vary depending on the chemical enviroment of the molecule and the molecular concentration. Molecular concentration also has an effect on the relative amplitudes of the two main absorption peaks [31]. The

absorption- and emission spectra of R6G in ethanol solution are shown in figure 6.

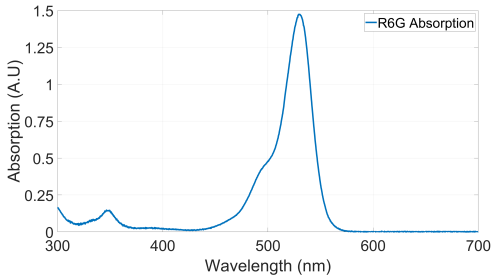

(a) R6G absorption in ethanol solution [32].

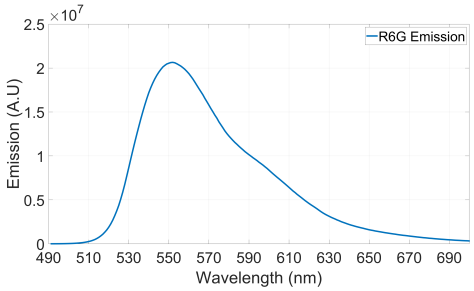

(b) R6G emission in ethanol solution [32].

Figure 6

The second most important material choice was the material of the cavity mirrors. To obtain efficient confinement of light, Q-factor of the cavity should be as high as possible.[4] Generally speaking high Q-factors require materials with high reflectivity, so the chosen material should have this characteristic. Another requirement for the mirror material comes from the active molecule, and its absorption. Since we want to confine light at the absorption wavelength of the active molecule the mirrors should be made of material which is highly reflective but doesn't absorb at that same wavelength. Given these restrictions the material of choice was selected to be silver. The absorption, reflectance and transmission curves of silver films of thickness 200 nm and 30 nm calculated using TMM are presented in figure 7.

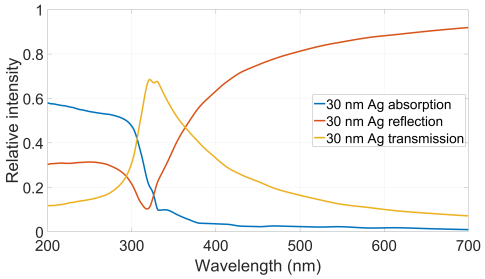

(a) 30 nm Ag film on top of semi infinite SiO2. Surrounding medium is air.

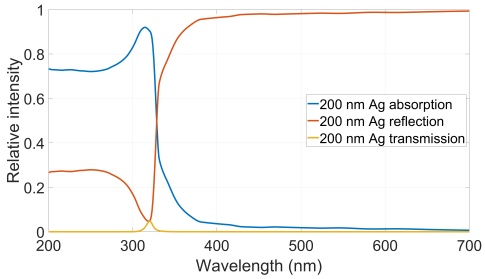

(b) 200 nm Ag film on top of semi infinite SiO2. Surrounding medium is air.

Figure 7

The material of the cavity spacer layer in between the mirrors was chosen to be PVA. PVA was chosen because its water soluble like R6G, so they can be easily mixed in spin

[4]There is however a practical limit for Q-factor. The limitation comes from the fact, that not only we want to achieve strong light-matter coupling, but also we want to be able to *measure* what comes out from the system as emission. If we increase the Q-factor too much then this becomes difficult as the cavity doesn't allow emission. This topic and the solution for the problem is discussed later in the context of cavity design.

solution. The refractive index of the spacer layer material affects the resonant wavelength of the cavity as can be seen from equation 13, so this has to be considered in sample design. The refractive index plot of PVA is shown in figure 8.

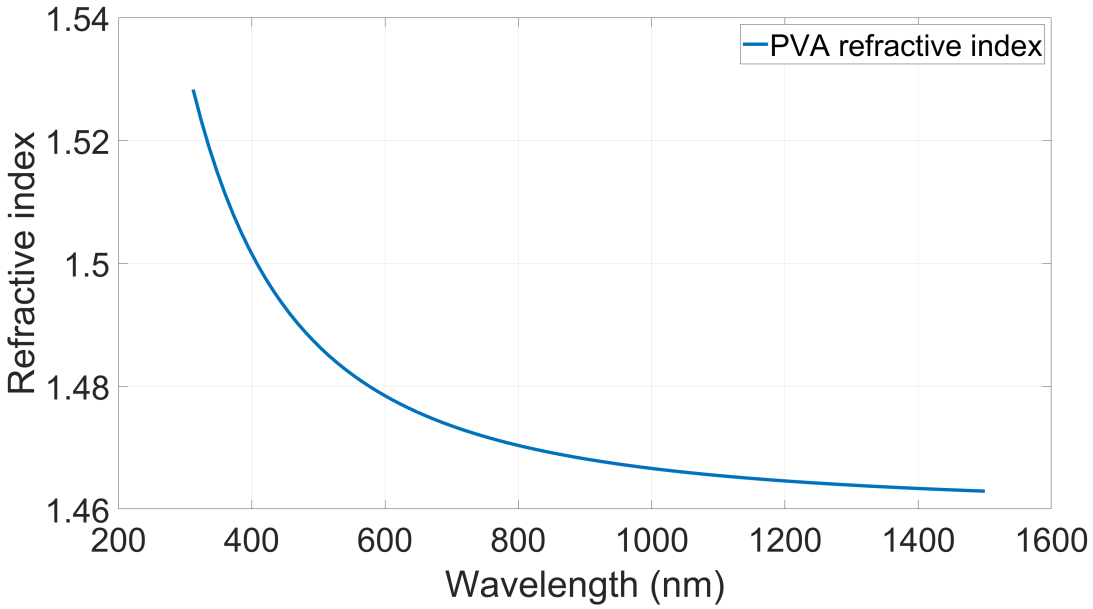

Figure 8. Refractive index of PVA obtained from [33], via [34].

The protective layer which is spin coated on top of the top mirror, was chosen to be poly methyl methacrylate (PMMA). As this layer is very thin, and located outside the actual cavity structure it doesn't affect to the cavity characteristics significantly.

After the materials of the cavity were chosen it was time to design the cavity geometry. To achieve high coupling strengths the cavity should be able to confine light as efficiently as possible. As explained earlier, efficient confinement of light requires high cavity Q-factor, which in turn requires highly reflecting cavity mirrors. As the mirror material was already chosen based on its reflection charecteristics, the only factor left having an effect on the mirror reflectivity was the thickness of the mirrors. At first thought it might sound like a good idea to make both mirrors very thick to maximize the reflectance. However, to be able to study the emission originating from the molecules *inside* the cavity we need to be able to measure what comes out from the cavity *trough* either one of the mirrors. This experimental restriction inspired the choice to use asymmetric cavity design with other mirror being very thick to maximize its reflection and another mirror thinner to allow some emission leak trough it. In the search for optimal mirror thicknesses many different cavity geometries were simulated using TMM and the best compromize between Q-factor and top mirror transmittance was achieved by using 200 nm bottom mirror and

30 nm top mirror. The optical charecteristics of the cavity mirrors are presented in figure 7 and the cavity absorption simulated using the chosen mirror thicknesses, and middle layer thickness maximizing the cavity absorption overlap with R6G absorption maxima at ~ 530 nm is shown in figure 3.

Spin solution preparation

The spin solution preparation started by dissolving the solid form R6G powder. In C1 millipore water was used as the only solvent, where as in C2 and C3 the R6G was dissolved in a mixture of millipore water and ethanol. The reason for using ethanol in C2 and C3 was that the solubility of R6G in ethanol is roughly four times that of water. To reach the concentrations used in C2 and C3 this was necessary, since otherways the amount of water in the spin solution would have decreased the viscosity so much that reaching the required film thickness with spin coating would have became impossible. After mixing the R6G powder and solvent the solubility was enhanched by first vortexing the solution for 3 min and then sonicating the vortexed solution for 30 to 60 min. After sonication the solution was inspected visually against a bright background light to check if there is any macroscopic undissolved particles. If undissolved particles could be found the sonication was continued until no macroscopic particles was found.

After the R6G was dissolved the R6G solution was mixed with 10 wt% PVA in millipore water. After mixing the solutions the resulting mixture was again vortexed for 3 min after which it was again sonicated for 30 to 60 min. The solutions made according to the previously explained steps were used as stock solutions which were then diluted with millipore water to make the final spin solutions. The amount of added water was determined by spin coating calibration test films with first using the undiluted solution, and later the already diluted solution and measuring thicknesses of the resulting films. The process was repeated diluting the stock solution further between each calibration sample until the film thickness was sufficiently close to the required target film thickness. The spin solution recipes used to fabricate the samples used in this thesis are summarized in table 1. The calculation for dry film concentrations shown in table 1 are presented in A.

Component	C1	C2	C3
R6G in stock solution	0.01426 g	0.04278 g	0.12834 g
H_2O in stock solution	2 mL	1.5 mL	1.5 mL
Ethanol in stock solution	-	2 mL	2 mL
10 wt% PVA in stock solution	2 mL	2 mL	2 mL
Stock solution to H_2O ratio in spin solution	1:1	2:1	4:6
Target concentration (dry film)	0.1920 mol/L	0.5761 mol/L	1.7282 mol/L
Spin speed (RPM)	2400	7000	1800

Table 1. Summary of the spin solution recipes, and spin speeds.

Sample fabrication

All samples were fabricated on a 20cm × 20cm BK7 glass piece. In the first step of the fabrication the glass pieces were cleaned carefully. First the glass pieces were submerged in acetone bath. After acetone bath the glasses were first rinsed with acetone, and then with isopropyl alcohol (IPA) after which the glasses were submerged in IPA bath and sonicated for 5 min. After sonication the glasses were again rinsed with IPA, after which they were quicly blown dry with dry nitrogen. Finally the cleaning was completed by inspecting the glass pieces visually for any macroscopic impurities.

After the cleaning the first step of the actual sample fabrication was the deposition of the 200 nm silver bottom mirror for both cavity- and mirror samples. The silver was deposited under ultra high vacuum (10^{-8} mbar) using a custom built electron beam evaporator. The evaporation rate was chosen to be $0.04 \pm 0.01\,\mathrm{nm\,s^{-1}}$ based on earlier studies on the effect of evaporation rate on the film surface roughness using the same electron beam evaporator [35].

After the deposition was completed the sample was immediately hurried to the spin coater which was used to deploy the molecule-resist layer on top of the bottom mirror. The reason for hurry in this step was to minimize the silver exposure to air, which is known to oxidise silver. Unlike spin coated films made of purely polymer, films consisting of both, polymer and active molecules were not fully reproducible even if the recipe for spin solution was kept unchanged. For this reason the correct spin speed for required film thickness was determined uniquely for each sample, based on a series of calibration samples from which the thickness was measured. The film thicknesses of the calibration samples were measured using KLA Tencor P-15 profilometer from a scratch made onto the films using a sharp scalpel. As this method destroys film in the process, the thickness of the actual sample couldn't be measured. For this reason the succesfulness of the sample

fabrication was not revealed until dispersion measurements, where the resonant wavelength of the cavity dependant on the film thickness (see eq. 13) could be seen. Because of the oxidisation concerns this time consuming spin speed calibration was done beforehand for each sample using the same spin solution that was used for the actual sample.

Using the predetermined spin speed the molecule-resist layer was spincoated on top of the bottom mirror. The corresponding film samples were fabricated parallelly, using the same spin coating parameters and spin solution that was used with the cavity samples. The spin speeds used to fabricate the samples used in this thesis are listen in table 1. Apart from spin speed, which was uniquely determined for each sample, every other parameter in the spin coating process was kept constant from sample to sample. The most important parameter was the spinning time, which was set to 3 min. After spin coating the samples were moved onto a hotplate set to 95 °C for 3 min to harden the spin coated layer. The temperature of the hotplate was monitored with external thermo meter to make sure that the temperature didn't fluctuate from the target temperature.

The fabrication process continued with the deposition of second silver mirror on top of the hardened molecule-resist layer. The silver deposition was performed exactly as described previously in the case of the bottom mirror, with the exception that instead of 200 nm target thickness the top mirror target thickness was only 30 nm.

Finally, the sample fabrication process was completed by spin coating a thin protection layer of 2 wt% PMMA, to prevent the top mirror from oxidisation. The actual thickness of this protection layer wasn't measured as the layer is located outside of the cavity, and thus has very little to no effect at all on the cavity characteristics. The spin coating parameters for this protection layer were kept constant troughout all the samples, and as the spin solution for this layer didn't contain anything apart from the polymer and its solvent (Chlorobenzene) it is safe to assume that the thickness of this layer didn't vary much amongst the produced samples. An illustrative figure presenting the not in scale cavity geometry is shown in figure 9.

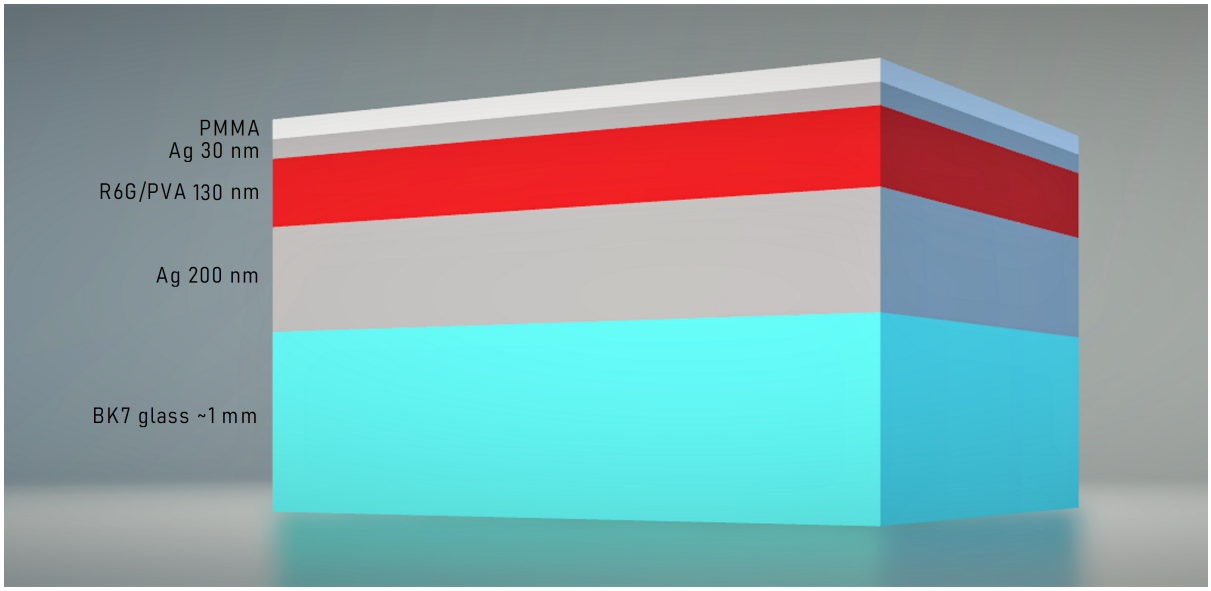

Figure 9. Not in scale illustration of the cavity geometry. Layers from top to bottom: $\sim$ 40 nm PMMA protective layer, 30 nm Ag top mirror, $\sim$ 130 nm R6G + PVA layer,200 nm Ag bottom mirror and 1 mm BK7 glass.

3.2 Measurements

The measurements performed for the purposes of this thesis include reflectance-, transmittance- and emission measurements. The first set of measurements performed for each cavity sample was the angle resolved reflectance measurement. Reflectance was measured at varying incident angles so that the dispersion of the reflectance could be observed. Because of the thick 200 nm bottom mirror all of the samples produced were non-transmitting. For this reason the absorption of each sample could be calculated using equation 10, simply by measuring the reflectance and setting $T = 0$. From the absorption spectra, the Rabi splitting can be observed as the absorption of the initially overlapped molecular absorption and cavity absorption split into two separate polariton absorption peaks. At the resonant angle, i.e., when the cavity mode and the molecular absorption are tuned, the magnitude of Rabi-split is given by equation 29 and the polariton absorption peaks separated by $\Omega_R/2$ symmetrically on both sides of the molecular absorption energy are equal in intensity.

In the second set of measurements the fluorescence of each cavity sample was measured. The fluorescence measurements were performed right after the dispersion measurement, without removing the sample from the sample holder in between the measurements. This was done to ensure, that the beam spot on the sample stays unchanged in between these measurements. The excitation was done using a laser with adjustable wavelength, and

the excitation wavelength was chosen such that for each cavity sample it matched the wavelength of the upper polariton absorption maxima at the resonance. The power of the laser pulses were monitored troughout the fluorescence measurement, and the resulting fluorescence values were normalized by the summed power values to make the fluorescence values comparable.

To have an uncoupled system reference data for the cavity measurements the reflectance, transmittance and emission of the film samples were measured. As the film samples were transmitting because of the lack of mirrors, transmittance measurement was necessary for determining the film absorption using equation 10. As the film samples don't have dispersion, all of the film measurements were performed for just a single angle.

Reflectance measurement

Prior to the reflectance measurement the halogen lamp white light source which was used to excite the sample in this measurement was set to its operating current of 4.3 A and let to warm up for an hour to let it stablize. The lamp was enclosed inside a housing equipped with optics to collimate the output light. The light beam was directed from the source into the sample by using reflective silver mirrors. Before reaching the sample the light was passed trough a polarizer set to pass s-polarized light and three iris diaphragms, which were used to attenuate the beam and control its size. The CCD camera and the monochromator were also kept on for atleast 15 min prior use to let them stabilize. After both the lamp and the CCD camera / monochromator combo were stabilized the lamp spectrum was collected, so it could be used to normalize the data from the actual reflectance measurement.

To perform the reflectance measurement the sample was mounted into a sample holder attached onto a manually operated rotation stage. Before the measurement the sample was aligned such that the normal to the sample surface was parallel to the incident light beam. This was done to ensure that the sample wasn't tilted which would cause systematic error to reflectance measurement. Additionally the sample position on the holder was tuned such that the sample itself, and the point where the beam hits the sample were on the axis of rotation of the rotation stage. This way the position where the beam hits the sample doesn't change when the incidence angle is varied.

For each cavity sample the reflectance was measured starting from incident angle of 10° to 70° with increments of 5°. The incident angle was measured from the normal of the sample surface. The light reflected from the sample was captured with a detector consisting of a collimating objective focusing the incident light into an optical fiber bundle.

The detector was mounted on a detector arm rotating coaxially with the rotation stage around the sample. The detection angle likewise to the incident angle was set manually. At each incident angle the detector was was set to an angle where the intensity of the reflected light was at its maximum. Ideally the angle of reflection would always be twice the angle of incident, but since the detector was very sensitive to the position and there is always some margin of error when setting the incident angle it was decided that the most reliable way of finding the correct angle of reflection is to search the position where the signal attains its maximum value. The collected signals were fed to an CCD camera / monochromator combo trough an optical fiber system. The CCD camera / monochromator combo was controlled by computer software. The measurement setup and beam path is shown in figure 10 and the equipment list corresponding to the numbering in figure 10 is listed in table 2.

The reflectance of the film samples was measured identically to the cavity sample reflectance, with the exeption that only single incident angle was used. The chosen incident angle was 10° and the corresponding detection angle was determined from the maximum signal intensity as described earlier in the context of cavity reflectance measurements.

Transmittance measurement

As was discussed earlier the transmittance measurement was necessary to perform in the case of film samples. Again likewise with the film reflectance measurement the transmittance measurement was performed only for 10° incident angle. The detector arm was set to detection angle of 180°, placing the detector to face the back side of the sample aligned with the optical axis. Again the lamp spectrum was collected to be used for normalizing the collected transmittance.

Fluorescence measurement

For the fluorescence measurement the excitation light was provided by a tunable laser instead of white light source. Before each measurement the laser was set on at least 15 min prior to the measurement to let it stabilize. The laser was directed into the setup trough an optical fiber. The beam's entrance from the fiber into the setup was controlled by a custom made beam shutter. The beam shutter was opened only for the brief period of time when the fluorescence signal was collected. This way the samples exposure to high intensity laser light was minimized reducing the amount of photobleahing. No significant photobleaching of the sample was observed during the measurements. After passing the shutter the beam was directed trough an aspheric lens used to collimate the beam, from

which the beam continued to beam sampler. The beam sampler redirects a fraction of the beam into the power meter, which measured the laser power during the time in which the shutter was opened. The majority of the beam continued from the beam sampler into a plano convex lens via two aluminium mirrors. From the lens the beam continued trough an iris diaphragm, a Glan laser polarizer set to pass s-polarized light and another iris diaphgram before finally reaching the sample [5]. The fluorescence signal coming from the sample was directed trough another Glan laser polarizer before reaching the detector optics. This polarizer was used to control the polarization of the detected signal. Both s- and p-polarized fluorescence was measured from each cavity sample. The collected fluorescence signal was passed into the CCD camera / monochromator combo trough an optical fiber. The measurement setup and beam path is again shown in figure 10 and the equipment list corresponding to the numbering in figure 10 is listed in table 2.

For the fluorescence measurement each cavity sample was excited at the incident angle corresponding to the resonant condition, at the wavelength matching the upper polariton absorption maxima. For the studied samples the excitation wavelengths λ_e and resonant angles θ_r were as follows: C1: $\lambda_e = 532\,\text{nm}$ and $\theta_r = 40$, C2: $\lambda_e = 483\,\text{nm}$ and $\theta_r = 30$ and C3: $\lambda_e = 448\,\text{nm}$ and $\theta_r = 10$. During the measurement the incident angle of the excitation light was kept constant but the detection angle was varied from 10° to 70° with increments of 5°. The detection angle was measured relative to the sample normal. The fluorescence of the film samples was collected only at detection angle of 15°, excited at the incident angle of 10°.

[5]The flip mirror labeled as component 4. in the figure 10 is flipped down away from the beam path during fluorescence measurements.

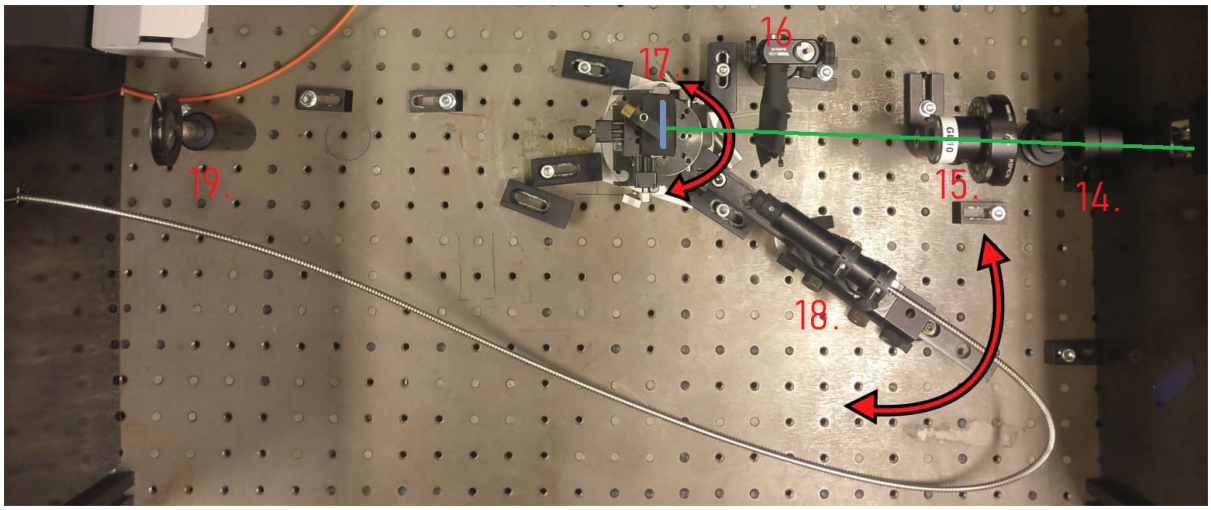

(a) Second part of the measurement setup. Illustration of the sample is shown in blue on the sample holder (component 17.) and the green line is showing the beam path (same for reflectance- and fluorescence measurement.) The red arrows are there to show how the sample stage (smaller arrow), and the detector arm (bigger arrow) can be rotated.

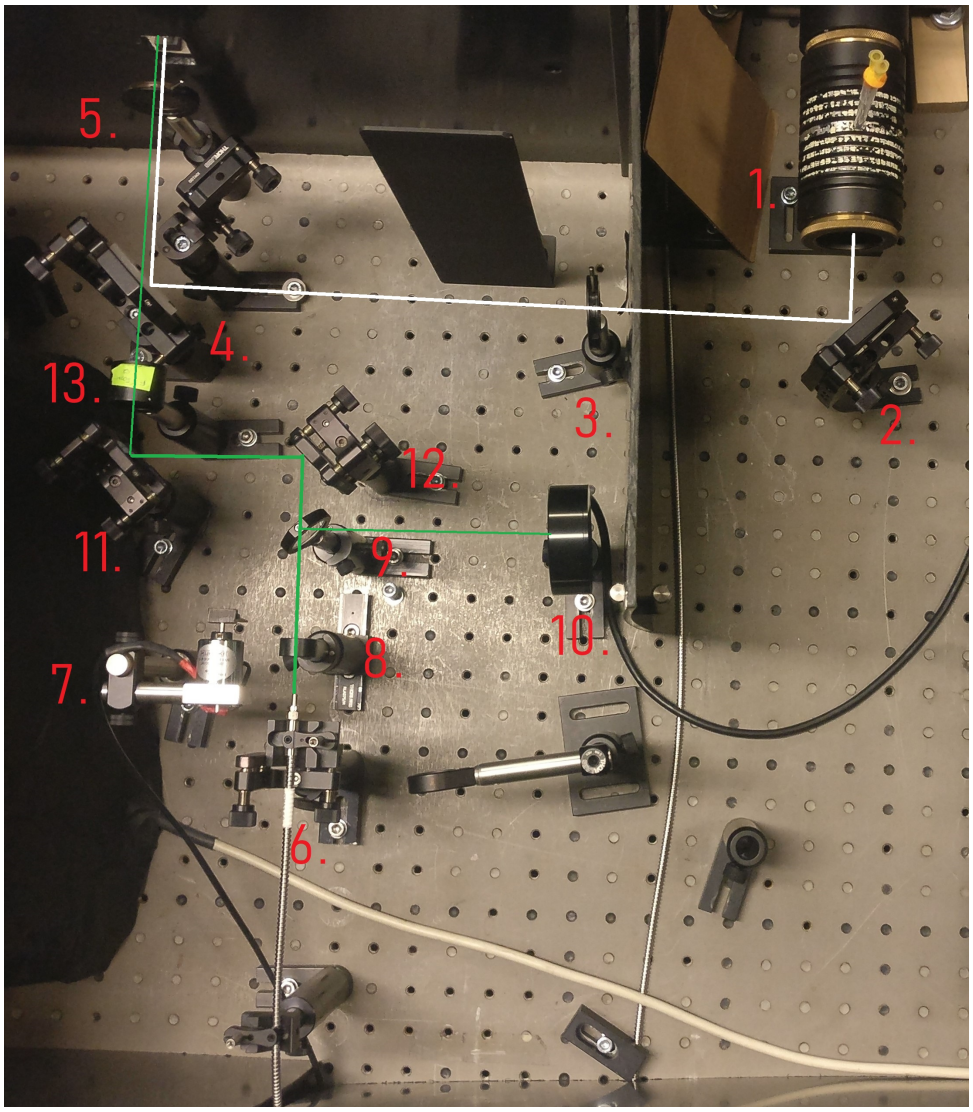

(b) First part of the measurement setup

Figure 10. The measurement setup with the beam paths higlighted for reflectance (white) and fluorescence (green). Details of the equipment can be seen from table 2

Equipment specific to the reflectance measurement		
No.	Component	Model
1.	Halogen lamp white light source	Oriel Lamp Housing / power supply ; 300 W Radiometric power supply
2.	Silver mirror	Thorlabs; PF20-03-P01
3.	Iris diaphragm	-
4.	Silver mirror	Thorlabs; PF20-03-P01
5.	Iris diaphragm	-
Equipment specific to the fluorescence measurement		
No.	Component	Model
6.	Laser light source	EKSPLA OPO NT230 series
7.	Custom made shutter	-
8.	Aspheric lens	Edmund Optics 47-728 15mm Dia., 0.33 Numerical Aperture, Uncoated, Aspheric Lens
9.	Beam sampler	ThorLabs BSF10-A, UV Fused Silica Beam Samplers (AR Coating: 350 - 700 nm)
10.	Laser power meter	Ophir PD10-C energy meter, Ophir USBI and the StarLab Version 3.40 Build 15 PC software
11.	Aluminium mirror	Thorlabs; PF10-03-F01
12.	Aluminium mirror	Thorlabs; PF10-03-F01
13.	plano convex lens	ThorLabs LA1908-AD=25.4 F=500.0mm N-BK7 A Coated Plano Convex Lens
-	Long pass filter (placed in front of the entrance slit of the monochromator)	Semrock EdgeBasic longpass 514 nm filter BLP01-514R-25
Universally used equipment		
14.	Lens holder (empty). Listed here for completeness.	-
15.	Glan laser polarizer set to pass s-polarized light	GL10, 10 mm Clear Aperture, Uncoated;
16.	Iris diaphragm	-
17.	Sample holder mounted on rotation stage	-
18.	Custom made light detector	The monochromator was fitted with a single leg fiber optic bundle (ThorLabs BFL200HS02, 2 meter, 250 to 1200 nm; Round-to-Linear Bundle, 7 x Ø200 µm Core Fibers, High-OH, SMA) and an custom made lens-based fiber optic interface with an adjustable rail system with two lens for correct f matching. Lens: Thorlabs LA1422-A, D=25.4, F=40.0, N-BK7, A Coated, Plano Convex Lens. Edmund Optics 88-725, 25.0mm Dia., 60.0mm FL, VIS-EXT Coated Plano-Convex Lens. A Semrock EdgeBasic longpass 514 nm filter (BLP01-514R-25) was inserted between the two rail lens (only for fluorescence measurement).
19.	Iris diaphragm	-
-	CCD camera	Andor IVAC CCD and Solis S software version 4.21.30007.0
-	Monochromator	Acton SP2150i and Acton Series Monochromator Control Software 5.2.4

Table 2. A list of components used in the experimental setup.

4 Results

In this chapter the experimentally obtained dispersion curves and fluorescence plots are presented. Additionally the theoretical truncated Tavis-Cummings model is fitted to the experimental dispersion curves.

4.1 Dispersion

The dispersion of absorption was determined for each cavity sample. Absorption was calculated from equation 10 by setting $T = 0$ and using the experimentally obtained reflectance values in place of R. Before using the reflectance values in equation 10 reflectance was normalized by the lamp spectrum to change the intensities from detector counts to relative intensities. Additionally the experimentally obtained absorption of a 185 nm silver mirror was deducted from the sample absorption to take in to account the light absorbed by the sample bottom mirror.

To fit the absorption data with the truncated Tavis-Cummings model the positions of polariton absorption peaks for each angle were determined. The positions were found by fitting a Voigt profile [36] to the experimental absorption data. The Voigt profile, which is a convolution of a Caychy- and an Gaussian distributions was fitted using a custom made Matlab script. The obtained polariton dispersion curves were given as an input to a custom made Matlab fitting script, which was used to fit the truncated Tavis-Cummings model to the polariton dispersion data. The script used Levenberg–Marquardt algorithm to compare the polariton dispersion obtained from the experimental data to the dispersion calculated using truncated Tavis-Cummings model, optimizing the collective coupling strength parameter g given by equation 27. As reported by M. A. Noginov et al. in their recent publication [31], the relative intensities of R6G main absorption peaks are strongly dependant on molecular concentrations. With the lowest concentration sample C1, the simple 2×2 truncated Tavis-Cummings Hamiltonian given by equation 28 was sufficient to fit the experimental data well. However when the concentration was increased in C2 and C3 the fittings using the 2×2 Hamiltonian, considering only the main absorption peak (530 nm) proved to be unsatisfactory and the 2×2 Hamiltonian was replaced by a 3×3 Hamiltonian [35, eq. 2.13] taking in to account the shoulder peak which is rising in intensity as the concentration is increased. As the 3×3 Hamiltonian is considering two

Rabi-splits occuring at both R6G absorption peaks the Hamiltonian also has two values for g corresponding to each absorption peak.

As shown by M. A. Noginov et al. [31] not only the intensities of the R6G absorption maxima, but also their position vary as a function of molecular concentration. For this reason different values for molecular absorption maxima were used in fittings for the experimental data obtained from different samples. For C1 the main absorption peak maximum that was used was at 535 nm. For C2 and C3 the absorption maxima of the shoulder- and main peaks were 506 nm and 556 nm and 519 nm and 569 nm respectively. Additionally in each fitting the the absorption maxima of the confined field were given as an input for the script. The values were extracted from the experimental dispersion of C4 by fitting a Gaussian profile to the experimental absorption spectrum at each incident angle. As the middle layer thickness of the cavities is not excactly same in the samples produced for this thesis, the fit was allowed to offset the inputted cavity dispersion in energy. This offset is a constant value added to each energy value at each incident angle, so the shape of the dispersion is not affected by it. The coupling strengths obtained from the peak to peak distance of the absorption maxima at the resonant angle correspond to the following Rabi-split energies: $\Omega_{R1} = 0.2518\,\text{eV}$, $\Omega_{R2} = 0.4836\,\text{eV}$ and $\Omega_{R3} = 0.6408\,\text{eV}$, where the numbering in the subscript corresponds to the sample in question. The corresponding coupling strengths obtained from the truncated Tavis-Cummings model fits were: $g^1_{C1} = 0.1123\,\text{eV}$, $g^1_{C2} = 0.1221\,\text{eV}$, $g^2_{C2} = 0.1625\,\text{eV}$, $g^1_{C3} = 0.0432\,\text{eV}$ and $g^2_{C3} = 0.3039\,\text{eV}$, where the subscript marks the sample in question and superscript is specifying the peak for which the coupling strength is considered (1 for shoulder- and 2 for main peak).

The resonant angles are estimated from the absorption 2d-plots as the angle where the upper- and lower polariton peaks are equal in height. Unfortunately the cavity of the sample C3 was a bit detuned so the resonant angle couldn't be accurately determined. Additionally in the case of C3 the upper polariton branch was exceeding energies of 2.9 eV at high angles which was the experimental limit of the setup in its current configuration. Because of this, the truncated Tavis-Cummings model could only be fitted for the angles below 45°. The experimental dispersion curves displaying a clear Rabi-split in all but the non-molecule-doped "empty" cavity reference system are shown in figures 11 and 12. For for the R6G-doped samples C1,C2 and C3 The Tavis-Cummings model fittings are overlaid on top of the experimental curves, and the resonant angles are shown for C1 and C2.

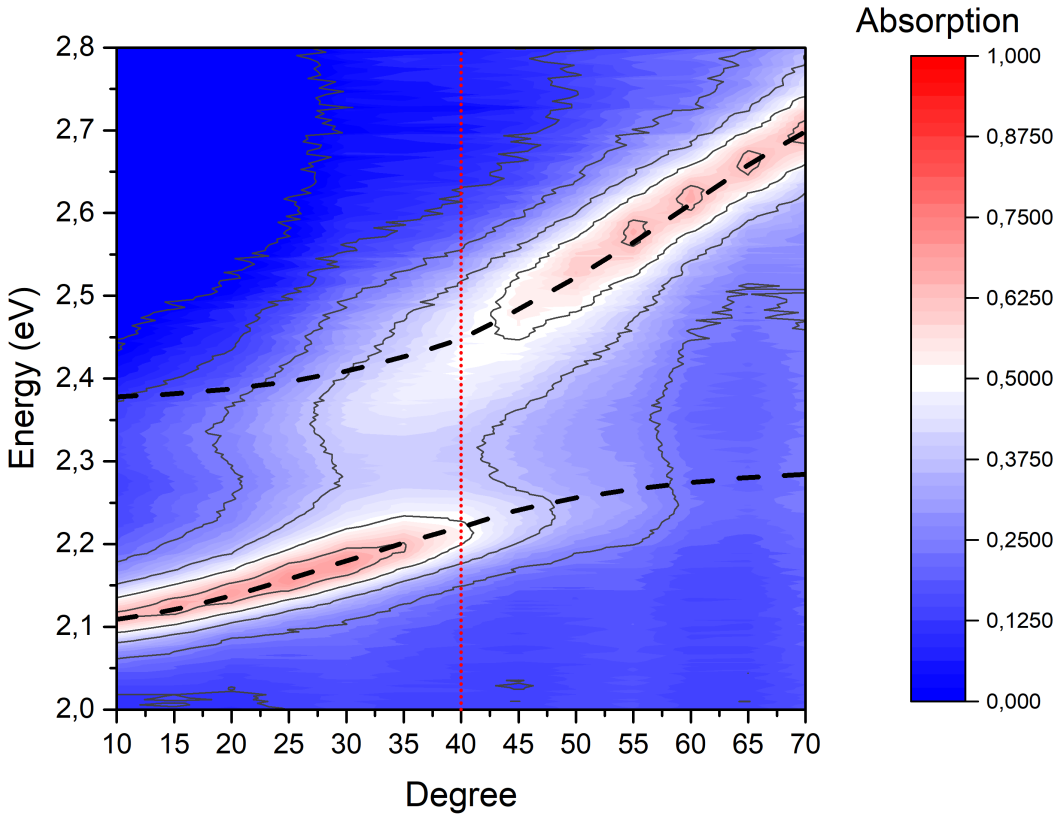

(a) C1 dispersion contour with Tavis-Cummings model fit (black dotted-line) and the resonant angle (red dotted-line).

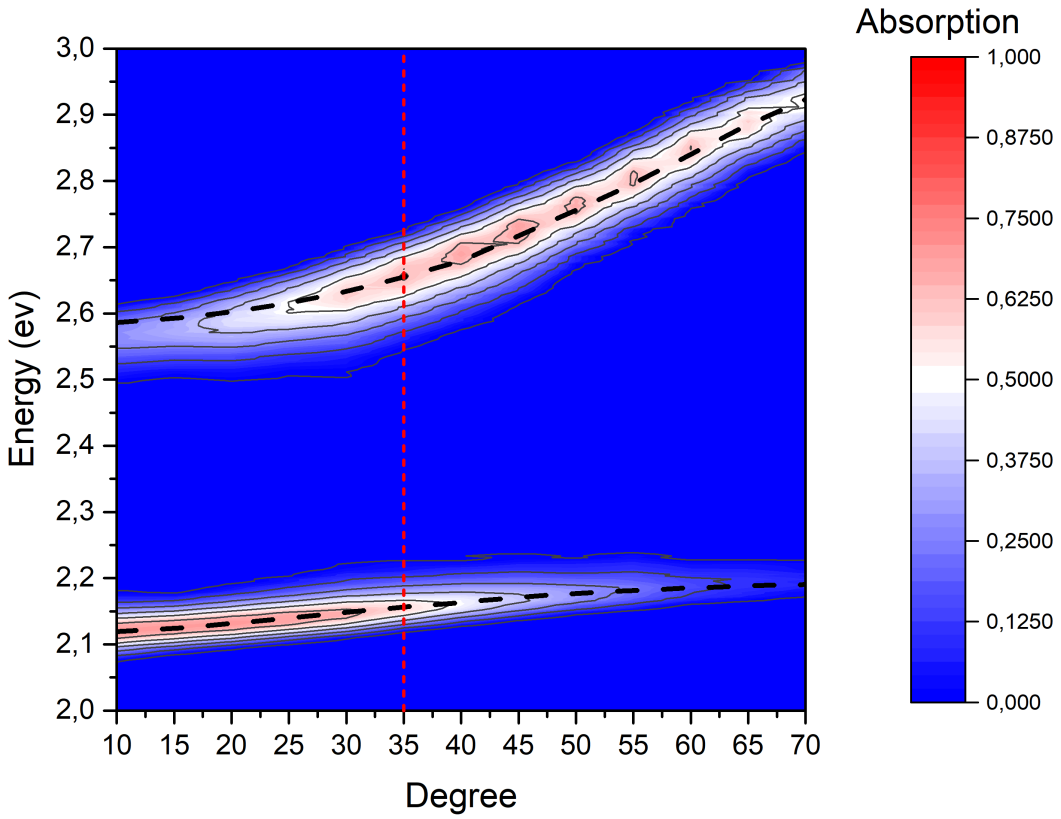

(b) C2 dispersion contour with Tavis-Cummings model fit (black dotted-line) and the resonant angle (red dotted-line).

Figure 11

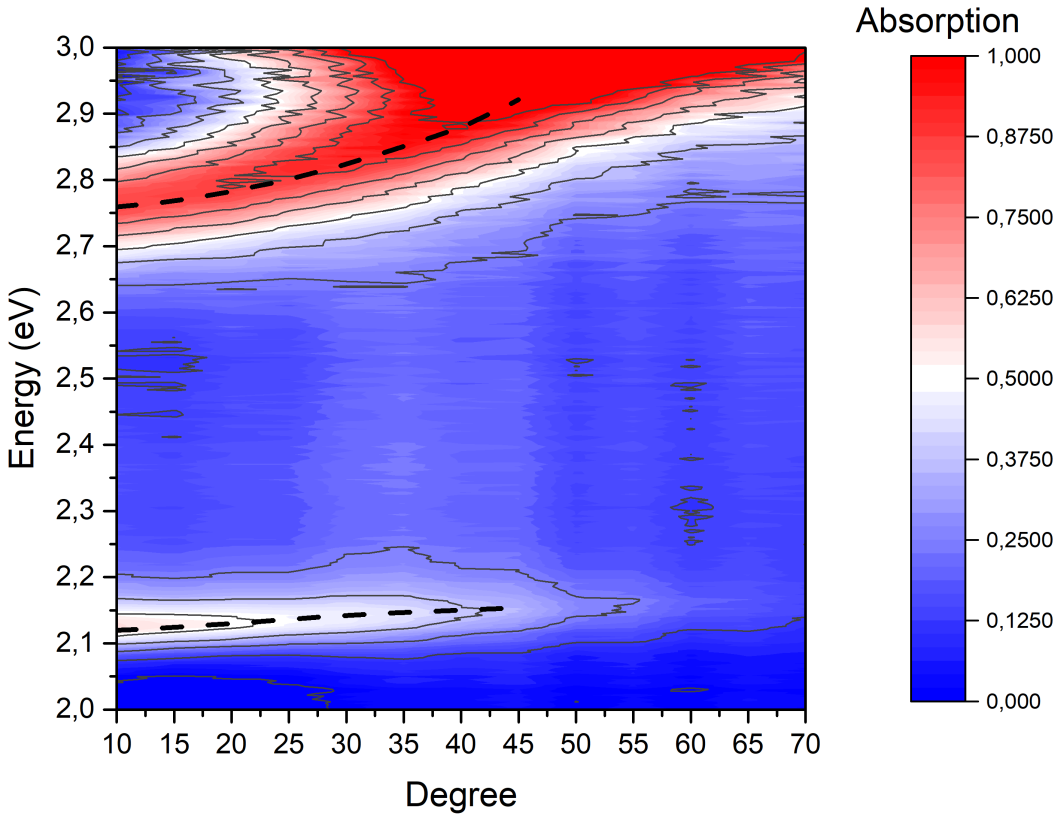

(a) C2 dispersion contour with Tavis-Cummings model fit (black dotted-line).

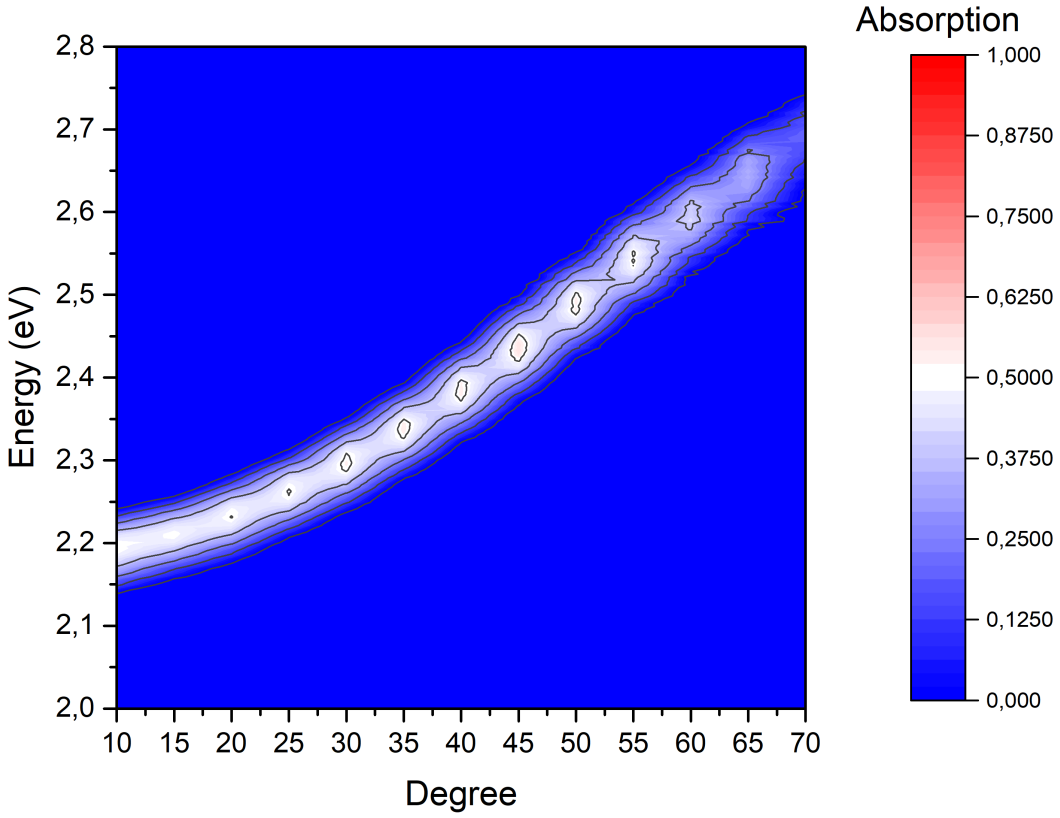

(b) C4 reference system dispersion contour

Figure 12

4.2 Film absorption

The film absorption was calculated using equation 10 using the experimentally acquired values for reflectance and transmittance. Again the absorption values were normalized with the lamp spectra to change the absorption values from absolute- to relative values.

From figure 12 it can be seen that the absorption is increasing as the molecular concentration is increased. This is to be expected as there is more molecules to absorb light in the case of higher concentrations. Another feature visible from figure 12 is the change of the spectral shape of the absorption. The shoulder peak at ~ 2.45 eV is seen to increase in intensity along with the increased molecular concentration in a similar fashion to what was reported by M. A. Noginov et al. [31].

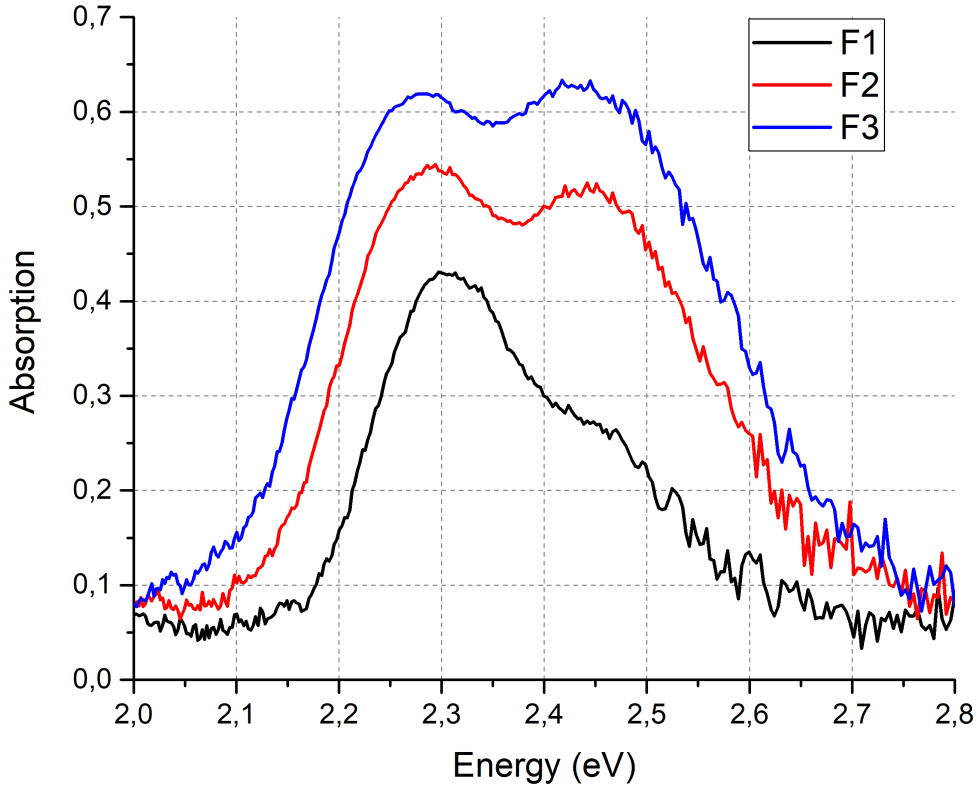

Figure 13. Absorption of F1,F2 and F3.

4.3 Cavity emission

The measured fluorescence values are normalized by dividing them with the absorption of the sample at the excitation wavelength, making the obtained emission intensities comparable between the samples, even if the actual molecular concentration is not known. Additionally the instrumental response of the experimental setup was taken into account as well as the Lambert's cosine law for the detection angle. The cavity emission plots detected at both s- and p-polarization at the resonant angle excited at the wavelength corresponding to the upper polariton absorption maximum are displayed in figures 14, 15 and 16.

As can be seen by comparing the emission measurements shown in figures 14,15 and 16 the emission maximum is located approximately at 2.1 eV in each measurement, roughly matching the lower polariton absorption maximum in the corresponding absorption measurement. The shape of the emission can also be seen following the lower polariton absorption dispersion curve. A trend of decreasing emission along with increased molecular contentration and coupling strength consequently can be seen by comparing the maximum emitted intensity at each measurement.

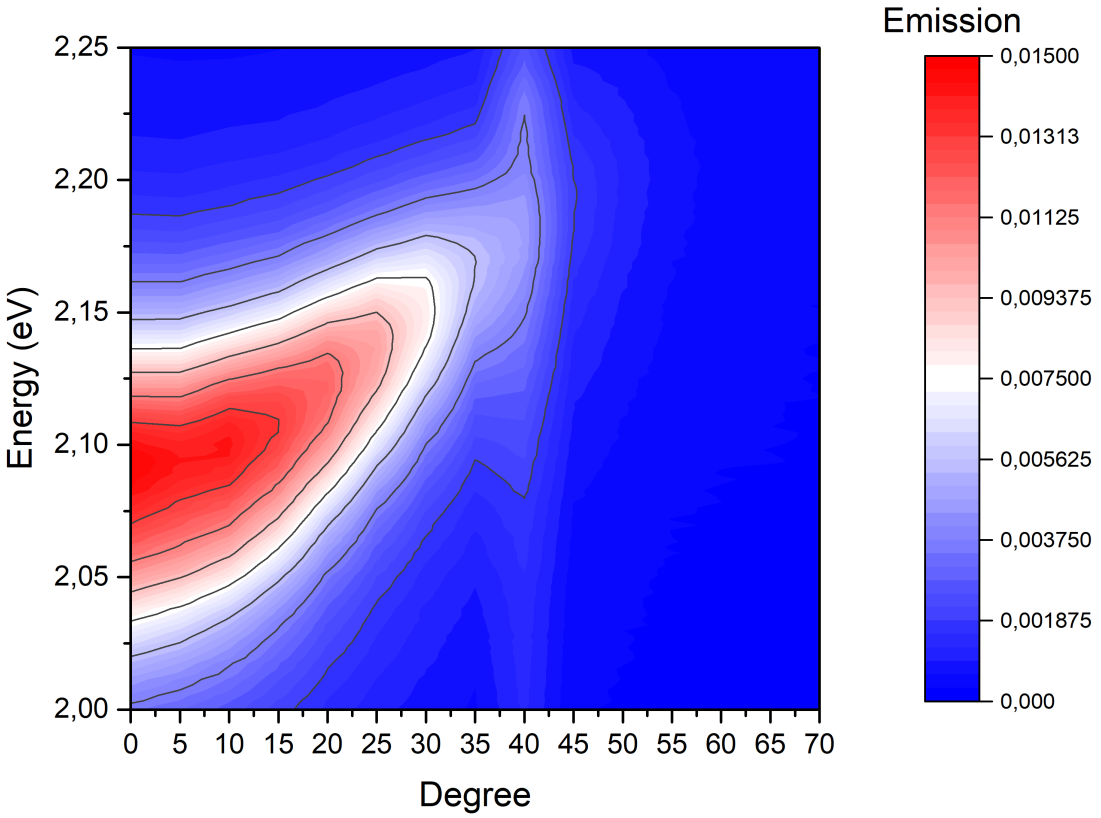

(a) S-polarized C1 emission.

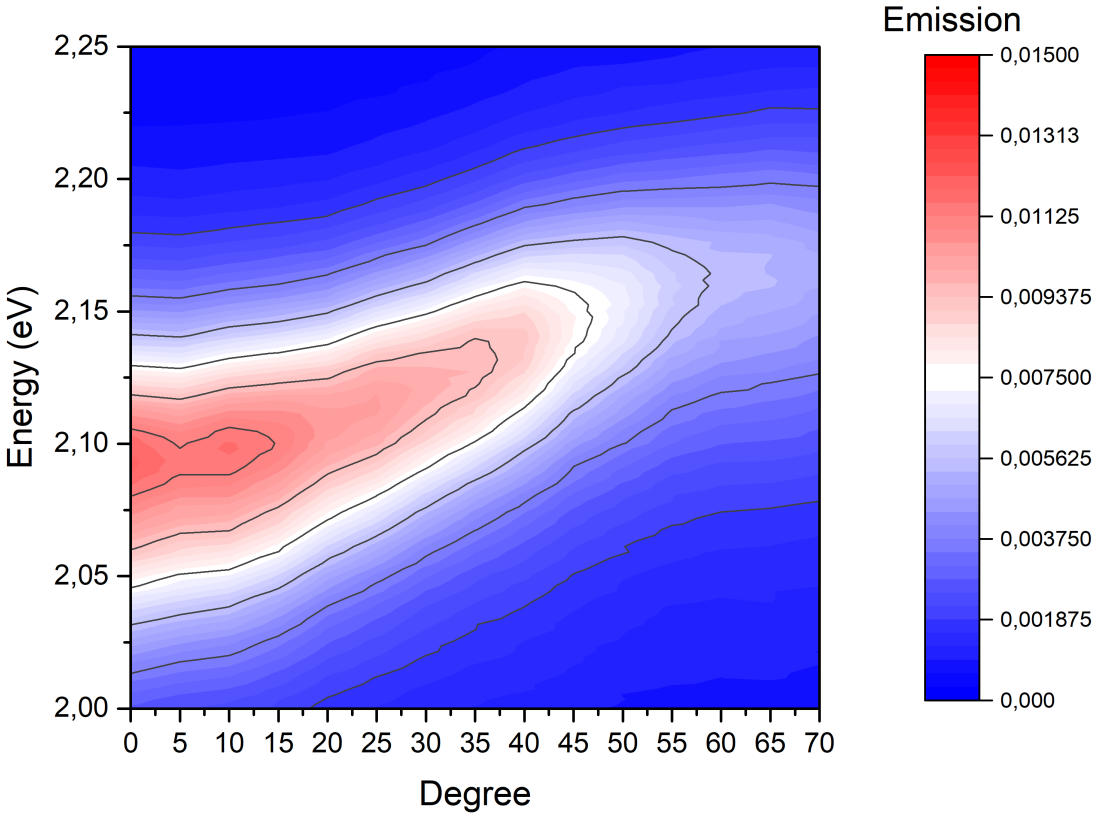

(b) P-polarized C1 emission.

Figure 14. C1 emission

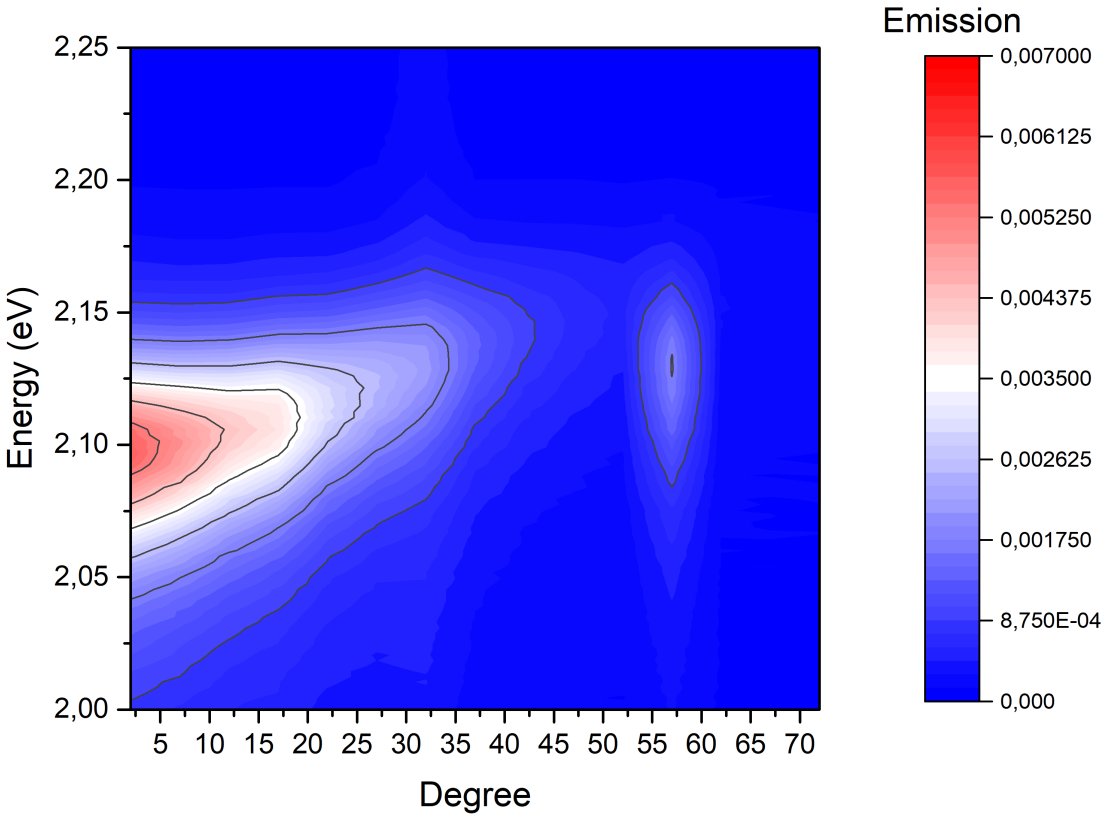

(a) S-polarized C2 emission.

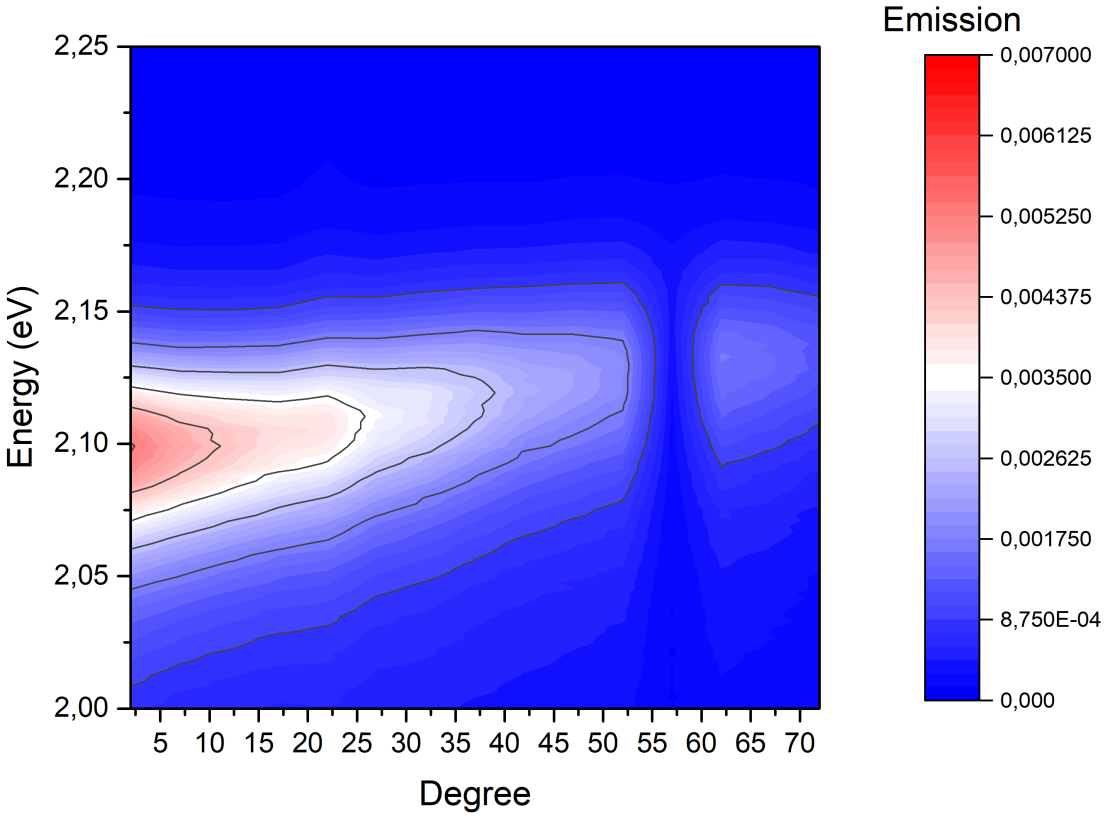

(b) P-polarized C2 emission.

Figure 15. C2 emission

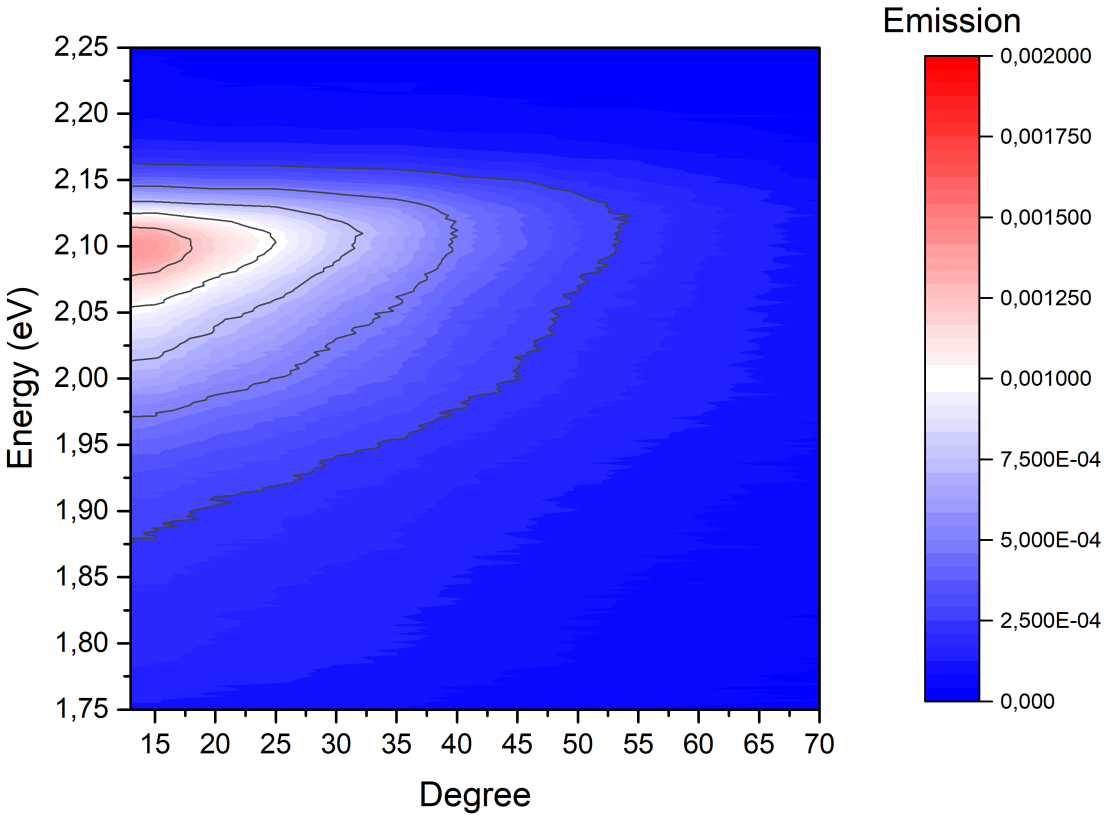

(a) S-polarized C3 emission.

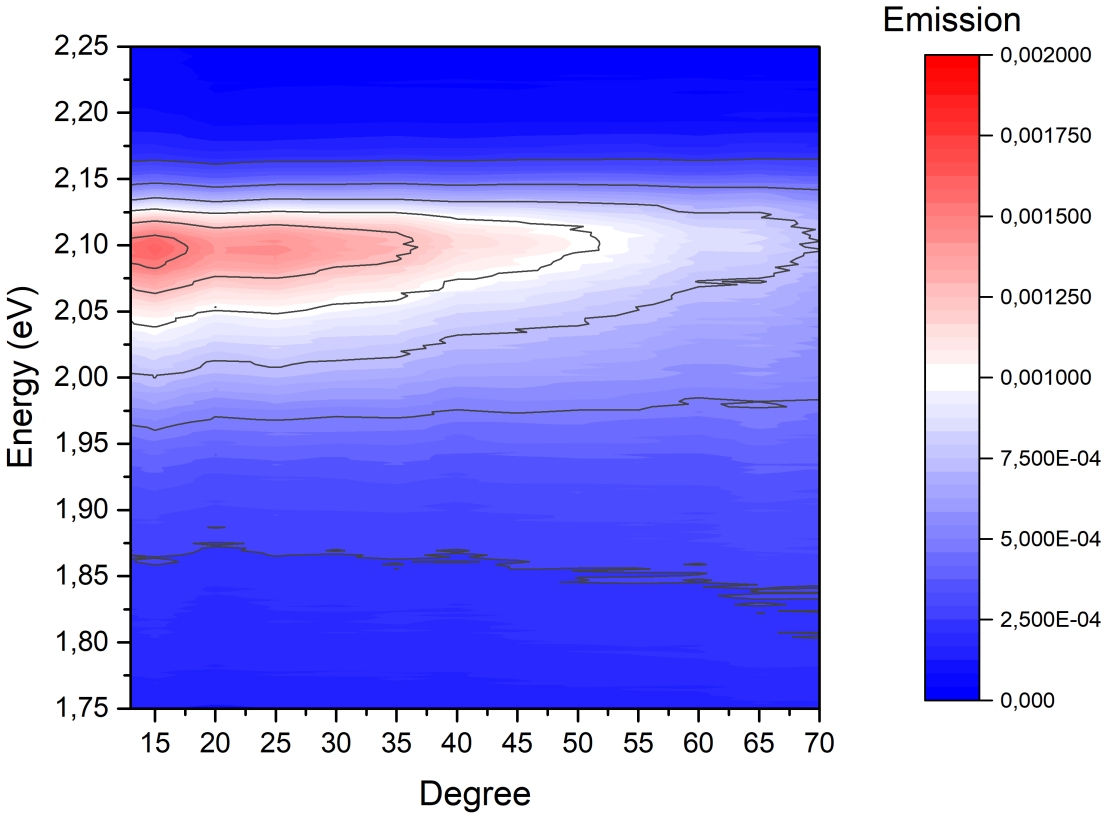

(b) P-polarized C3 emission.

Figure 16. C3 emission

4.4 Film emission

Likewise with the cavity samples the film fluorescence values were normalized by the absorption at the excitation wavelength to make the obtained emission values comparable to each other. To make the film emission trend comparable with the emission trend observed from cavity samples was a bit more tricky, because in the case of the cavity samples the emission was filtered by the cavity absorption. To make the film- and cavity emission trends comparable the convolutions of the corresponding film emission and cavity absorptions were calculated for each sample. For the convolution the film emissions excited at 10° and detected at 15° was used with the corresponding cavity absorption at 15° incident angle. The film emission and the convoluted film emission and cavity absorptions are presented in figure 17.

As can be seen from figure 17 the film emission, and convolution of the film emission and cavity absorption are both decreasing as the molecular concentration is increased. This implies that the fluorescence is quenching at high concentrations. In the case of the convolution of C2 and F2 the intensities can be seen to drop below 0 in certain regions. This is an computational artifact induced by the convolution calculation, and doesn't represent any physical phenomenon. The rate of the emission decrease along with the increased concentration, determined from the maximum intensities of each sample can be seen to be slightly different in the cases of regular emission, and convoluted emission. Accurate comparison of the convoluted emissions however is difficult here because of the uncertainty induced by the convolution itself, and for that reason the emission decrease rate along with molecular concentration increase cannot be accurately determined.

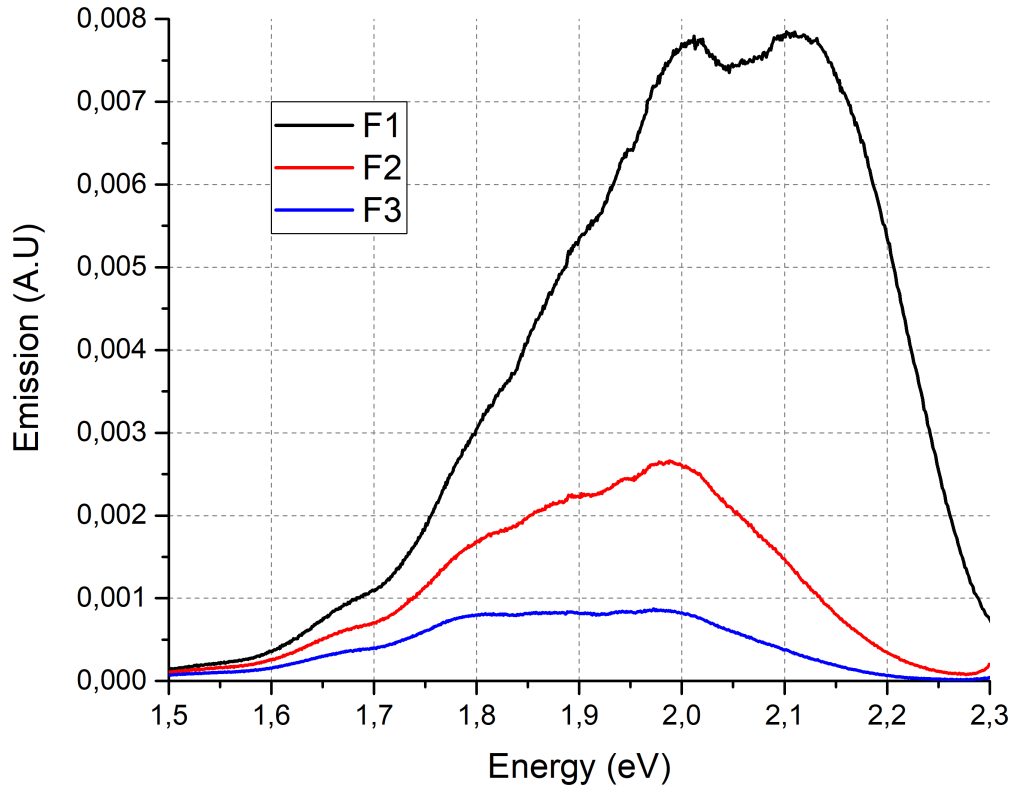

(a) Emissions of F1, F2 and F3.

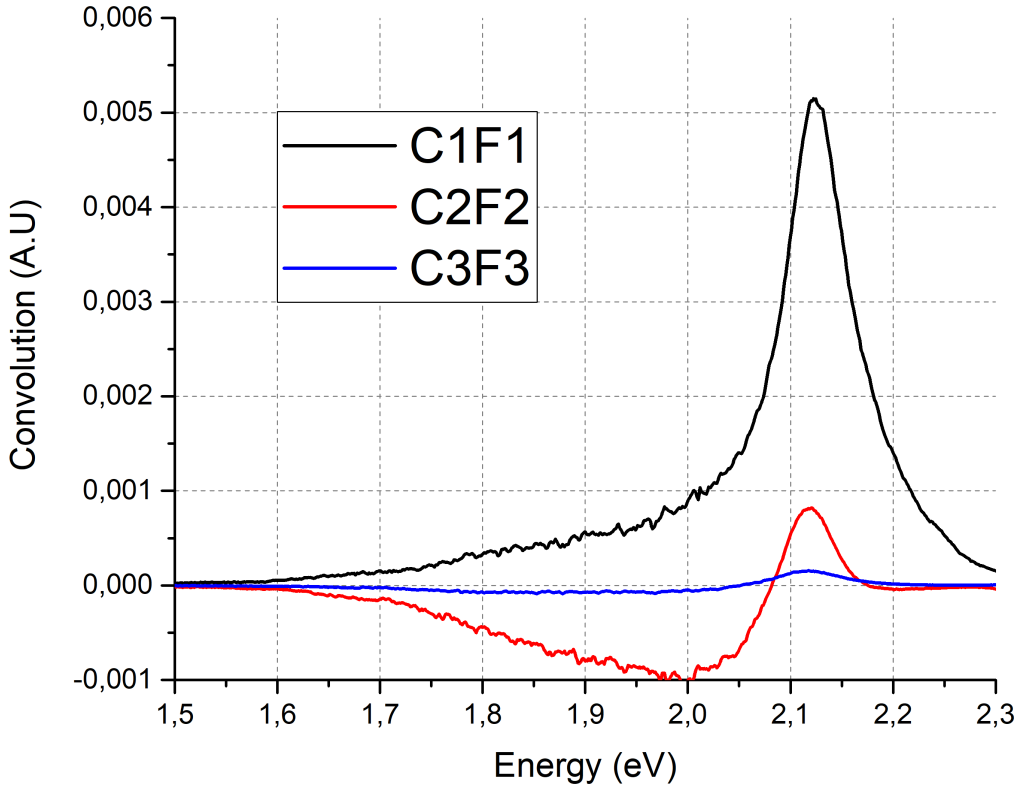

(b) Convolutions of F1/C1, F2/C2 and F3/C3.

Figure 17

5 Conclusions

In this study the emission evolution of a strongly coupled system was studied over a range of coupling strengths extending from strong- to ultra-strong coupling regime. Using the coupling strengths g calculated from the observed Rabi-split values using equation 29 and ω_c of sample C4 at the resonant angle summed with the free energy parameter optimized by the fitting program, the ratios $\frac{g}{\omega_c}$ for the studied samples are: C1: 0.0536, C2: 0.0971 and C3: 0.1278, putting C1 and C2 into strong coupling regime and C3 in the ultra strong coupling regime as per the definition given in the end of chapter 2. As can be seen from figures 11 and 12 the polariton dispersion curves obtained from the fit are nicely matching the experimental dispersion, suggesting that the used truncated Tavis-Cummings model is adequate to model the systems used in this study. The greatest uncertainty of the reported coupling strengths comes in the case of C3 where the resonant condition couldn't be accurately determined because of the detuned cavity, and because the fit couldn't be used to trace the full experimental dispersion because of the experimental limitations. Another uncertainty in the fittings and in the coupling strengths extracted from them, affecting all of the studied samples comes from the fact that the fit was allowed to vary both molecular absorption maxima- and the cavity dispersion energy. The latter is an unavoidable nuisance because to determine the actual resonant wavelength of the cavity sample one would need to measure the thickness of the cavity middle layer destroying the sample in the process. The molecular absorption however was measured experimentally from the reference films with the results shown in figure 13. Unfortunately these measurements were carried out after the fits were done, and because of time restrictions the fits could not be redone using the experimental molecular absorption maxima.

The fit-optimized absorption maxima values converted into eV were as follows: C1: 2.31746 eV, C2: 2.4517 eV and 2.2174 eV, C3: 2.3882 eV and 2.1627 eV. As can be seen by comparing the molecular absorption maxima determined by the fit, and the experimental absorption maxima in figure 13 we can see that in the case of C1 and C2 they are very similar but not so much in the case of C3. This is to be expected, since this fit had the greatest uncertainty because of the ill defined resonance angle. Similar trend can be seen in resonant angles determined by the fit as the crossing point between molecular absorption of the R6G main peak and the cavity dispersion which again apart from

C3 are in reasonable agreement with the reported resonant angles determined from the experimental 2d polariton absorption spectra as is shown in appendix B, giving further evidence that the model used for fitting here is modelling the coupled system realistically.

By studying the evolution of the polariton dispersion curves from figures 11 and 12 one can observe a trend of flattening polariton dispersion curves along with the increased coupling strength, a charecteristic of a ultra strongly coupled system [37]. This flattening is especially distinguishable in the case of lower polariton branch.

From the cavity emission measurements shown in figures 14, 15 and 16 one can observe that the emission is roughly matching the lower polariton absorption in shape and in energy, suggesting that the lower polariton branch is offering a pathway for relaxation for the coupled system. A systematic feature present in all of the emission measurements is that the most intense emission is coming from lowest part of the lower polariton branch. This is to be expected since by emitting from there the system can relax into the lowest possible energy state.

Whereas the shape of the emission can be understood from the energy dynamics of a coupled system, the trend of decreasing emission along with increased molecular concentration and coupling strength is not something that one would necessarily expect. By adopting a simplified view of the situtation one could expect to see more emission coming from the samples with increased amount of fluorescing molecules. However as organic molecules such as the R6G used in this study tends to form aggregates at high concentrations some amount of emission quenching is to be expected, as the samples used here are very highly concetrated. By looking at the film emissions and teir convolutions in figure 17 one can see that the above assumption is correct, as the trend of decreasing emission along with increasing concentration is reproduced in these reference system samples.

The rate at which this emission decrease is happening when the concentration is increased however seems to be slightly different in the case of the cavity samples and film samples implying that strongly coupling the system might have some effect into the system's emission. By comparing the maximal emitted intensities of the cavity samples to the convoluted film emissions in figures 18 and 17 one can see that in the case of cavity samples the emission is decreasing roughly by a factor of three as the target concentration is increased by a factor of three. In the case of the convoluted emission the same increase in concentration is seemingly decreasing the emission roughly by a factor of five suggesting that the emission is decreasing faster in the uncoupled reference system than in the coupled system. However to verify this assumption one would need a more sophisticated

way to compare the emission trends seen here in film- and cavity samples.

To summarize the main results of this thesis the evolution of the absorption dispersion and emission of the coupled system was studied over range of coupling strengths from strong- to ultra strong coupling regime. The emission can be seen to trace the lower polariton absorption branch suggesting that this is the preferred relaxation pathway for the coupled system. Also evident from the emission measurements is the decreased emission along with increased molecular concentration. This however is caused by the fluorescence quenching of the extremely highly concetrated samples, and is not related to the physics of light-matter coupling. To study the effect of increasing coupling strength on the system's emission further one should aim at even higher coupling strengths as the highest concentrated sample studied here - C3 is just barely reaching the ultrastrong coupling regime, and the possible effects that the ultrastrong coupling might have on the system's emission might still be too subtle to be detected. Additionally a more careful study on the decrease rate of the emission along with the increased concentration could provide new information on how the coupling is affecting the system's emission. The main results of this thesis are summarized in figure 18 displaying the Rabi-split energies determined from the polariton peak to peak distances of absorption 2d-plots and emission of the cavity samples as a function of target concentration. Additionally shown are the "theoretical" coupling strengths estimated from the coupling strength of C1 determined from peak to peak distance. This coupling strength value is used along with the target concentration in equation 29 to estimate the splits of higher concentrated C2 and C3 when N is increased by a factor of three in between each successive sample corresponding to the difference in target molecular consentration between the samples.

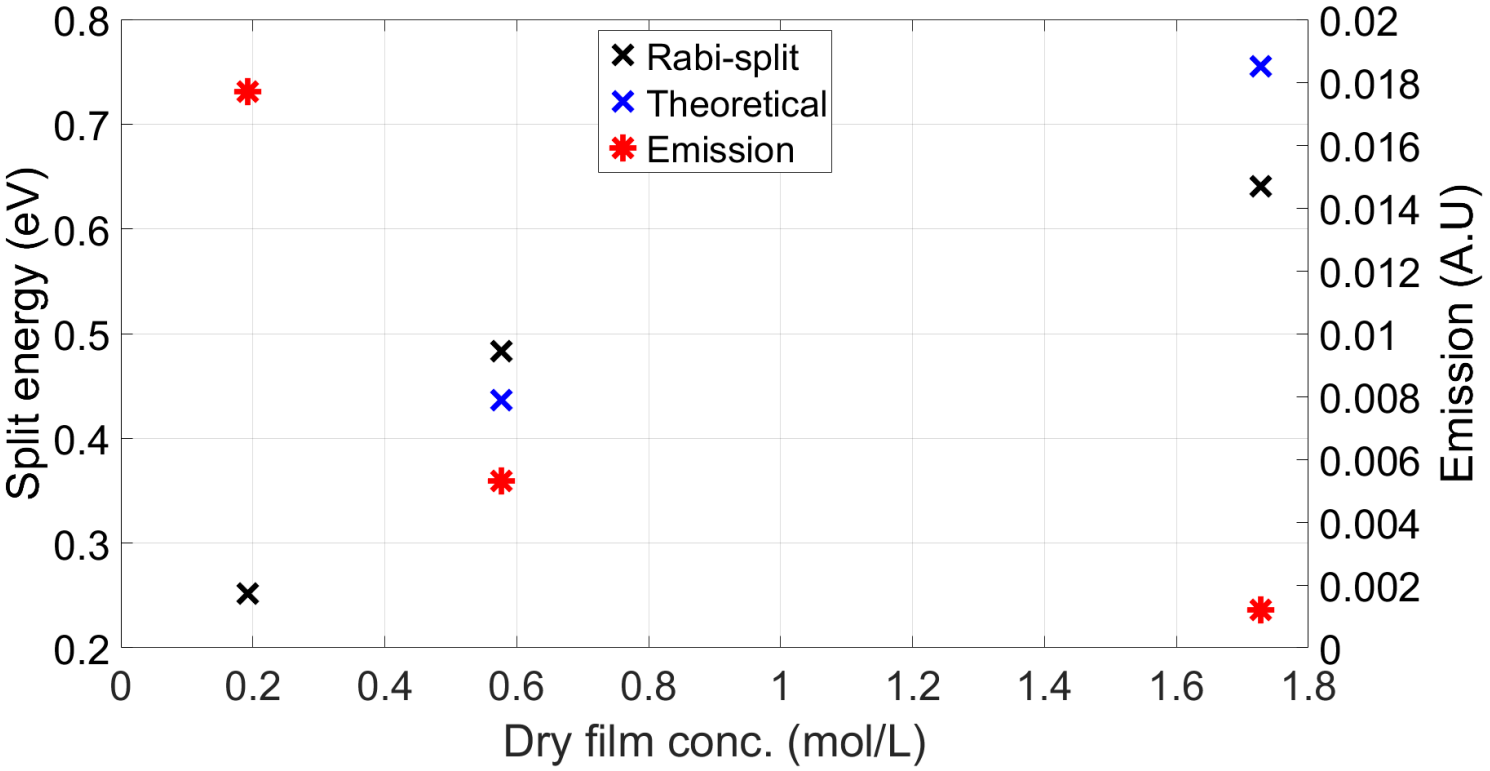

Figure 18. Summary of the results shown in this thesis.

References

[1] E. M. Purcell, H. C. Torrey, and R. V. Pound, "Resonance absorption by nuclear magnetic moments in a solid", *Phys. Rev.*, vol. 69, pp. 37–38, 1-2 Jan. 1946. DOI: 10.1103/PhysRev.69.37. [Online]. Available: https://link.aps.org/doi/10.1103/PhysRev.69.37.

[2] J. A. Hutchison etc. "Modifying chemical landscapes by coupling to vacuum fields", *Angewandte Chemie International Edition*, vol. 51, no. 7, pp. 1592–1596, 2012. DOI: https://doi.org/10.1002/anie.201107033. eprint: https://onlinelibrary.wiley.com/doi/pdf/10.1002/anie.201107033. [Online]. Available: https://onlinelibrary.wiley.com/doi/abs/10.1002/anie.201107033.

[3] X. Zhong etc. "Non-radiative energy transfer mediated by hybrid light-matter states", *Angewandte Chemie (International ed. in English)*, vol. 55, no. 21, pp. 6202–6206, May 2016, ISSN: 1433-7851. DOI: 10.1002/anie.201600428. [Online]. Available: https://doi.org/10.1002/anie.201600428.

[4] K. Georgiou etc. "Control over energy transfer between fluorescent bodipy dyes in a strongly coupled microcavity", *ACS Photonics*, vol. 5, no. 1, pp. 258–266, 2018. DOI: 10.1021/acsphotonics.7b01002. eprint: https://doi.org/10.1021/acsphotonics.7b01002. [Online]. Available: https://doi.org/10.1021/acsphotonics.7b01002.

[5] A. Shalabney etc. "Coherent coupling of molecular resonators with a microcavity mode", *Nature Communications*, vol. 6, no. 1, Jan. 2015, ISSN: 2041-1723. DOI: 10.1038/ncomms6981. [Online]. Available: http://dx.doi.org/10.1038/ncomms6981.

[6] K. M. Birnbaum etc. "Photon blockade in an optical cavity with one trapped atom", *Nature*, vol. 436, no. 7047, pp. 87–90, Jul. 2005, ISSN: 1476-4687. DOI: 10.1038/nature03804. [Online]. Available: http://dx.doi.org/10.1038/nature03804.

[7] Y. K. Wang and F. T. Hioe, "Phase transition in the dicke model of superradiance", *Phys. Rev. A*, vol. 7, pp. 831–836, 3 Mar. 1973. DOI: 10.1103/PhysRevA.7.831. [Online]. Available: https://link.aps.org/doi/10.1103/PhysRevA.7.831.

[8] T. J. Milburn, M. S. Kim, and M. R. Vanner, "Nonclassical-state generation in macroscopic systems via hybrid discrete-continuous quantum measurements", *Physical Review A*, vol. 93, no. 5, May 2016, ISSN: 2469-9934. DOI: 10.1103/physreva.93.053818. [Online]. Available: http://dx.doi.org/10.1103/PhysRevA.93.053818.

[9] A. Frisk Kockum etc. "Ultrastrong coupling between light and matter", *Nature Reviews Physics*, vol. 1, Jan. 2019. DOI: 10.1038/s42254-018-0006-2.

[10] A. Bayer etc. "Terahertz light–matter interaction beyond unity coupling strength", *Nano Letters*, vol. 17, Sep. 2017. DOI: 10.1021/acs.nanolett.7b03103.

[11] E. T. Jaynes and F. W. Cummings, "Comparison of quantum and semiclassical radiation theories with application to the beam maser", *Proceedings of the IEEE*, vol. 51, no. 1, pp. 89–109, Jan. 1963, ISSN: 1558-2256. DOI: 10.1109/PROC.1963.1664.

[12] V. Yakovlev, V. Nazin, and G. Zhizhin, "The surface polariton splitting due to thin surface film lo vibrations", *Optics Communications*, vol. 15, no. 2, pp. 293–295, 1975, ISSN: 0030-4018. DOI: https://doi.org/10.1016/0030-4018(75)90306-5. [Online]. Available: http://www.sciencedirect.com/science/article/pii/0030401875903065.

[13] V. Agranovich, H. Benisty, and C. Weisbuch, "Organic and inorganic quantum wells in a microcavity: Frenkel-wannier-mott excitons hybridization and energy transformation", *Solid State Communications*, vol. 102, no. 8, pp. 631–636, 1997, ISSN: 0038-1098. DOI: https://doi.org/10.1016/S0038-1098(96)00433-4. [Online]. Available: http://www.sciencedirect.com/science/article/pii/S0038109896004334.

[14] *Sciencedirect strong coupling*, https://www.sciencedirect.com/search/advanced?qs=strong%20coupling, Accessed: 2020.03.21.

[15] I. G.
bibinitperiod W. Phillips, *Electromagnetism*. University of Manchester: Wiley, 2004.

[16] B. Harbecke, "Coherent and incoherent reflection and transmission of multilayer structures", *Applied Physics B*, vol. 39, no. 3, pp. 165–170, Mar. 1986, ISSN: 1432-0649. DOI: 10.1007/BF00697414.

[17] J. Peatross and M. Ware, *Physics of Light and Optics*. https://optics.byu.edu/home, 2015.

[18] *Lumerical - fabry-perot cavity*, https://support.lumerical.com/hc/en-us/articles/360042323754-Fabry-Perot-cavity-INTERCONNECT-, Accessed: 2020.03.21.

[19] *Q factor*, https://www.rp-photonics.com/q_factor.html, Accessed: 2020.03.21.

[20] Anonymous, "Proceedings of the american physical society", *Phys. Rev.*, vol. 69, pp. 674–674, 11-12 Jun. 1946. DOI: 10.1103/PhysRev.69.674.2. [Online]. Available: https://link.aps.org/doi/10.1103/PhysRev.69.674.2.

[21] X. Li etc. "Effective modal volume in nanoscale photonic and plasmonic near-infrared resonant cavities", *Applied Sciences*, vol. 8, no. 9, p. 1464, Aug. 2018, ISSN: 2076-3417. DOI: 10.3390/app8091464. [Online]. Available: http://dx.doi.org/10.3390/app8091464.

[22] M. Hertzog etc. "Strong light–matter interactions: A new direction within chemistry", *Chem. Soc. Rev.*, vol. 48, pp. 937–961, 3 2019. DOI: 10.1039/C8CS00193F. [Online]. Available: http://dx.doi.org/10.1039/C8CS00193F.

[23] *The electromagnetic field*, https://ocw.mit.edu/courses/nuclear-engineering/22-51-quantum-theory-of-radiation-interactions-fall-2012/lecture-notes/MIT22_51F12_Ch10.pdf, Accessed: 2020.03.21.

[24] S. Haroche and D. Kleppner, "Cavity quantum electrodynamics", *Physics Today*, vol. 42, no. 1, pp. 24–30, 1989. DOI: 10.1063/1.881201. eprint: https://doi.org/10.1063/1.881201. [Online]. Available: https://doi.org/10.1063/1.881201.

[25] M. Yurkin and A. Hoekstra, "The discrete dipole approximation: An overview and recent developments", *Journal of Quantitative Spectroscopy and Radiative Transfer*, vol. 106, pp. 558–589, Jul. 2007. DOI: 10.1016/j.jqsrt.2007.01.034.

[26] F. Arbeloa etc. "Photoresponse and anisotropy of rhodamine dye intercalated in ordered clay layered films", *Journal of Photochemistry and Photobiology C: Photochemistry Reviews*, vol. 8, pp. 85–108, Oct. 2007. DOI: 10.1016/j.jphotochemrev.2007.03.003.

[27] K. Fujii, *Introduction to the rotating wave approximation (rwa) : Two coherent oscillations*, 2014. arXiv: 1301.3585 [quant-ph].

[28] J. Gyamfi, *An introduction to the holstein-primakoff transformation, with applications in magnetic resonance*, Jun. 2019.

[29] Y. Wang and J. Y. Haw, "Bridging the gap between the jaynes–cummings and rabi models using an intermediate rotating wave approximation", *Physics Letters A*, vol. 379, no. 8, pp. 779–786, Apr. 2015, ISSN: 0375-9601. DOI: 10.1016/j.physleta.2014.12.052. [Online]. Available: http://dx.doi.org/10.1016/j.physleta.2014.12.052.

[30] A. Frisk Kockum etc. "Ultrastrong coupling between light and matter", *Nature Reviews Physics*, vol. 1, no. 1, pp. 19–40, Jan. 2019, ISSN: 2522-5820. DOI: 10.1038/s42254-018-0006-2. [Online]. Available: http://dx.doi.org/10.1038/s42254-018-0006-2.

[31] C. On etc. "Effect of molecular concentration on spectroscopic properties of poly(methyl methacrylate) thin films doped with rhodamine 6g dye", *Opt. Mater. Express*, vol. 7, no. 12, pp. 4286–4295, Dec. 2017. DOI: 10.1364/OME.7.004286. [Online]. Available: http://www.osapublishing.org/ome/abstract.cfm?URI=ome-7-12-4286.

[32] *R6g spectra*, https://omlc.org/spectra/PhotochemCAD/html/083.html, Accessed: 2020.03.21.

[33] M. J. Schnepf etc. "Nanorattles with tailored electric field enhancement", *Nanoscale*, vol. 9, pp. 9376–9385, 27 2017. DOI: 10.1039/C7NR02952G. [Online]. Available: http://dx.doi.org/10.1039/C7NR02952G.

[34] *Pva refractive index*, https://refractiveindex.info/?shelf=organic&book=polyvinyl_alcohol&page=Schnepf, Accessed: 2020.03.21.

[35] S. V. Baieva, "Strong coupling between surface plasmon polaritons and sulforhodamine 101 dye", *Nanoscale Research Letters*, vol. 7, no. 191, Mar. 2012, ISSN: 1556-276X. DOI: 10.1186/1556-276X-7-191. [Online]. Available: https://doi.org/10.1186/1556-276X-7-191.

[36] *Voigt line shape fit*, https://se.mathworks.com/matlabcentral/fileexchange/57603-voigt-line-shape-fit, Accessed: 2020.03.21.

[37] S. Kéna-Cohen, S. A. Maier, and D. D. C. Bradley, "Ultrastrongly coupled exciton–polaritons in metal-clad organic semiconductor microcavities", *Advanced Optical Materials*, vol. 1, no. 11, pp. 827–833, 2013. DOI: https://doi.org/10.1002/adom.201300256. eprint: https://onlinelibrary.wiley.com/doi/pdf/10.1002/adom.201300256. [Online]. Available: https://onlinelibrary.wiley.com/doi/abs/10.1002/adom.201300256.

[38] J. Casanova etc. “Deep strong coupling regime of the jaynes-cummings model”, *Phys. Rev. Lett.*, vol. 105, p. 263 603, 26 Dec. 2010. DOI: 10.1103/PhysRevLett.105.263603. [Online]. Available: https://link.aps.org/doi/10.1103/PhysRevLett.105.263603.

[39] S. De Liberato, “Light-matter decoupling in the deep strong coupling regime: The breakdown of the purcell effect”, *Phys. Rev. Lett.*, vol. 112, p. 016 401, 1 Jan. 2014. DOI: 10.1103/PhysRevLett.112.016401. [Online]. Available: https://link.aps.org/doi/10.1103/PhysRevLett.112.016401.

[40] *Quantization of the free electromagnetic field: Photons and operators*, https://www.phys.ksu.edu/personal/wysin/notes/quantumEM.pdf, Accessed: 2020.03.21.

[41] *Rhodamine 6g*, https://pubchem.ncbi.nlm.nih.gov/compound/Rhodamine-6G, Accessed: 2020.03.21.

A Dry film concentration

The target concentration of the molecular films used in cavity- and film samples was calculated using equation A.1

$$C = \frac{m_{R6G}/M_{R6G}}{m_{PVA}/\rho_{PVA}} = \frac{m_{R6G}}{m_{PVA}} \left(\frac{\rho_{PVA}}{M_{R6G}} \right), \tag{A.1}$$

where m_{R6G} is the mass of the R6G molecule used in each sample (0.0143 g for C1/F1, 0.0428 g for C2/F2 and 0.12834 g for C3/F3), $M_{R6G} = 479\,\mathrm{g/mol}$, $m_{PVA} = 0.2$ g is the estimated mass of the solid PVA and $\rho_{PVA} = 1.29\,\mathrm{g/mL}$.

Using the above mentioned values in equation A.1 yields the following sample concentrations:

- $C_{C1/F1} = 0.1920\,\mathrm{mol/L}$
- $C_{C2/F2} = 0.5761\,\mathrm{mol/L}$
- $C_{C3/F3} = 1.7282\,\mathrm{mol/L}$

B Truncated Tavis-Cummings fits

The following graphs are displaying the truncated Tavis-Cummings fits along with the absorption maxima extracted from the experimental absorption. Additionally shown are the resonant angles and molecular absorptions.

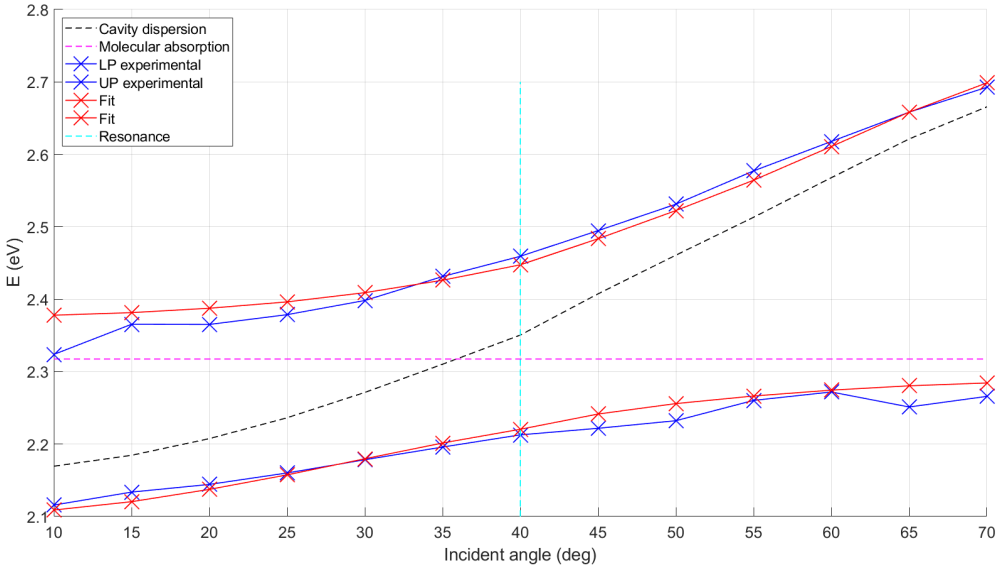

Figure B.1. Truncated Tavis-Cummings model fit to C1.

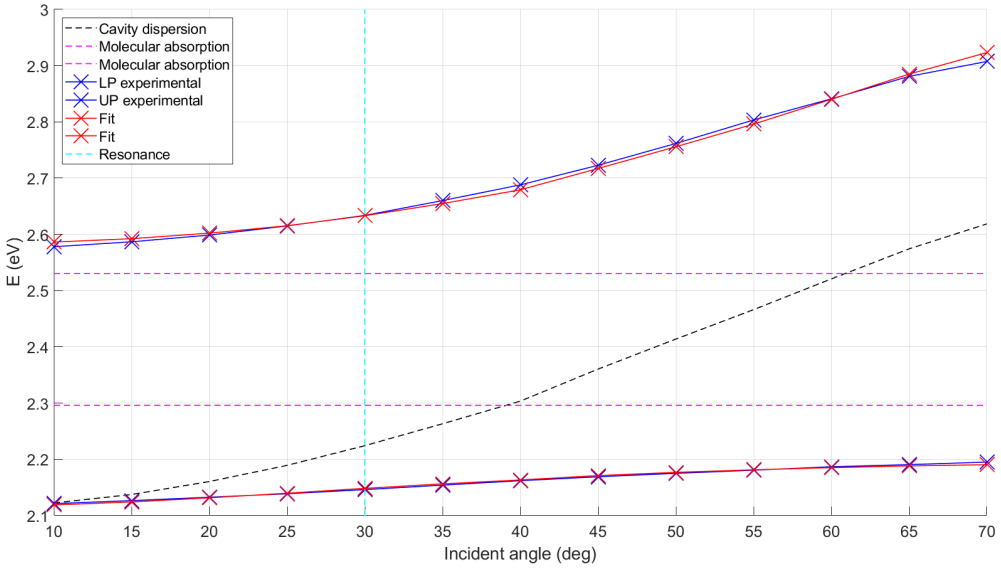

Figure B.2. Truncated Tavis-Cummings model fit to C2.

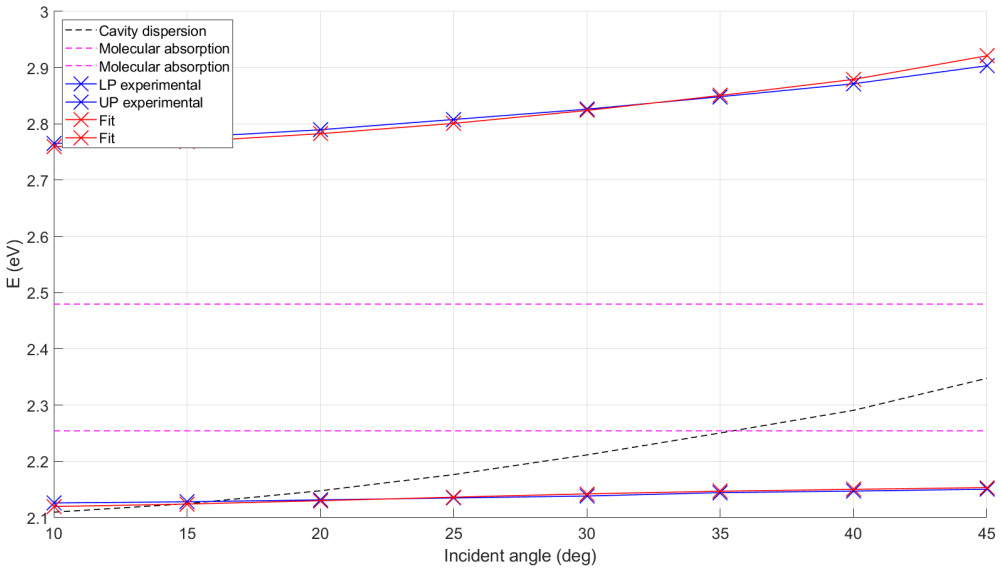

Figure B.3. Truncated Tavis-Cummings model fit to C3.